Journal of Medicinal Chemistry

Repurposing a Library of Human Cathepsin L Ligands: Identification of Macrocyclic Lactams as Potent Rhodesain and Trypanosoma brucei Inhibitors

Maude Giroud, Uwe Dietzel, Lilli Anselm, David Banner, Andreas Kuglstatter, Jörg Benz, Jean-Baptiste Blanc, Delphine Gaufreteau, Haixia Liu, Xianfeng Lin, August Stich, Bernd Kuhn, Franz Schuler, Marcel Kaiser, Reto Brun, Tanja Schirmeister, Caroline Kisker, François Diederich, and Wolfgang Haap

J. Med. Chem., **Just Accepted Manuscript** • DOI: 10.1021/acs.jmedchem.7b01869 • Publication Date (Web): 29 Mar 2018

Repurposing a Library of Human Cathepsin L Ligands: Identification of Macrocyclic Lactams as Potent Rhodesain and *Trypanosoma brucei* Inhibitors

Maude Giroud,[†,#] Uwe Dietzel,[‡,#] Lilli Anselm,[°] David Banner,[°] Andreas Kuglstatter,[°] Jörg Benz,[°] Jean-Baptiste Blanc,[°] Delphine Gaufreteau,[°] Haixia Liu, Xianfeng Lin, August Stich,[Δ] Bernd Kuhn,[°] Franz Schuler,[°] Marcel Kaiser,[§,¥] Reto Brun,[§,¥] Tanja Schirmeister,[||] Caroline Kisker,[‡] François Diederich,[†] Wolfgang Haap[°]**

[†]Laboratorium für Organische Chemie, ETH Zurich, Vladimir-Prelog-Weg 3, 8093 Zurich, Switzerland

[‡]Rudolf-Virchow Center for Experimental Biomedicine, University of Würzburg, Josef-Schneider-Strasse 2, 97080 Würzburg, Germany

[°]Roche Pharmaceutical Research and Early Development (pRED), Roche Innovation Center Basel, F. Hoffmann-La Roche Ltd., Grenzacherstrasse 124, 4070 Basel, Switzerland

Roche Pharma Research and Early Development, Roche Innovation Center Shanghai, 720 Cailun Road, Pudong, Shanghai 201203, China

[Δ]Department of Tropical Medicine, Medical Mission Institute, Salvatorstrasse 7, 97074 Würzburg, Germany

[§]Swiss Tropical and Public Health Institute, Socinstrasse 57, 4051 Basel, Switzerland

[¥]University of Basel, Petersplatz 1, 4003 Basel, Switzerland

[||]Institut für Pharmazie und Biochemie, Johannes Gutenberg-Universität Mainz, Staudinger Weg 5, 55128 Mainz, Germany

KEYWORDS. macrocycle – rhodesain – trypanosome – sleeping sickness – cysteine protease – human African trypanosomiasis – drug repurposing – target repurposing.

ABSTRACT: Rhodesain (RD) is a parasitic, human cathepsin L (hCatL) -like cysteine protease produced by *Trypanosoma brucei* (*T. b.*) species and a potential drug target for the treatment of human African trypanosomiasis (HAT). A library of hCatL inhibitors was screened, and macrocyclic lactams were identified as potent RD inhibitors (K_i < 10 nM), preventing the cell-growth of *T. b. rhodesiense* (IC_{50} < 400 nM). SARs addressing the S2 and S3 pockets of RD were established. Three cocrystal structures with RD revealed a non-covalent binding mode of this ligand class, due to oxidation of the catalytic Cys25 to a sulfenic acid (Cys–SOH) during crystallization. The P-glycoprotein efflux ratio was measured and the *in vivo* brain penetration in rats determined. When tested *in vivo* in acute HAT model, the compounds permitted up to 16.25 (vs. 13.0 for untreated controls) mean days of survival.

INTRODUCTION

Human African trypanosomiasis (HAT or African sleeping sickness) is a protozoan infection caused by two subspecies of *Trypanosoma brucei* (*T. b.*): *T. b. gambiense*, responsible for the chronic form of HAT, and *T. b. rhodesiense*, responsible for the more acute form of the disease.[1] The third subspecies, *T. b. brucei*, causes Nagana disease in cattle.[1] HAT can be divided into two clinical stages, the haemolymphatic stage, which, if left untreated, progresses into stage 2, the neurological stage.[2,3] To date, only five drugs against this pathogen are available, the most recent development being the nifurtimox-eflornithine (NECT) combination therapy, launched by the Drugs for Neglected Diseases *initiative* (DND*i*) in 2009, and recommended by WHO thereafter.[4] Because of the severe side effects of these drugs, research towards the development of novel compounds is urgently required.[5–9] In the field of neglected tropical diseases (NTDs), it is common to initiate industrial–academic partnerships,[10,11] where compounds or targets are repurposed from previous drug programs.[12] Such partnerships notably led to fexinidazole[13,14] and oxaborole (SCYX-7158),[15,16] which are currently in clinical trials and close to the verge of being introduced in clinical use.[17]

Parasitic cysteine proteases have emerged as attractive targets for drug discovery due to their indispensable roles in disease propagation.[18,19] Bloodstream *Trypanosoma brucei* parasites express two papain family cysteine proteases: the human cathepsin L (hCatL)-like rhodesain (RD) and an hCatB-type enzyme TbCatB, with overlapping activity profiles.[20–22] RD is involved in the parasite's iron homeostasis,[23] in performing the turnover of variant surface glycoproteins,[24,25] in degrading the host immunoglobulins,[26] and might help the parasite to cross the blood-brain barrier (BBB).[26] RD is structurally highly similar to hCatL,[27] a potential drug

target against diabetes, atherosclerosis and abdominal aortic aneurysms,[28] various cancers,[29–31] and Alzheimer's disease.[32]

Based on the structural similarities of hCatL and RD, a library of 49 hCatL inhibitors, designed for a metabolic disease campaign at F. Hoffmann-La Roche Ltd., was screened against RD. Herein, we report the identification of macrocyclic ligands, such as **1** and **2**, as potent, trypanocidal RD inhibitors, with already good drug-like properties. Efforts towards their further derivatization and the optimization of pharmacokinetic (PK) properties were deployed. Using structure-based drug design (SBDD), the macrocycles were optimized towards higher selectivities for RD versus hCatL (the compounds tested so far did not inhibit other human cathepsins, such as B, K, S, and V). In addition, three crystal structures of macrocycles in complex with RD (PDB IDs: 6EX8, 6EXO, and 6EXQ), which add valuable structural information to the two existing RD crystal structures (PDB IDs: 2P7U[33], 1.6 Å resolution and 2P86[22], 1.16 Å resolution), are reported, together with 3 crystal structures of macrocycles in complex with hCatL (PDB IDs: 6EZP, 6EZX, and 6F06). Brain penetration,[34] which is crucial for targeting stage 2 HAT, was evaluated in *in vitro* and *in vivo* assays. At last, selected macrocycles were tested in acute *in vivo* HAT models.

RESULTS AND DISCUSSION

Hit Identification. A series of 49 structurally diverse hCatL inhibitors,[35] provided by F. Hoffmann-La Roche Ltd., was tested in a fluorometric assay against the cysteine protease RD.[36–38] Out of 49 ligands, 44 hits for RD with inhibitory constants $K_i < 0.5$ μM were identified, among them 24 compounds with $K_i < 0.01$ μM. These hits belong to two different ligand classes: proline-based inhibitors, already reported in the context of halogen bonding in the S3 pocket of

hCatL,[39] and macrocycles.[35] The most potent hits were tested in a first screen against the parasite *T. b. brucei* in an Alamar® blue assay[40] to evaluate their ability to inhibit *in vitro* cell-growth (Figure S1). The macrocyclic series **1–18**[35] (Table S1), among them 5 compounds with IC_{50} values < 0.4 μM and no observable cytotoxicity (rat myoblast L-6 cells, IC_{50}-values > 50 μM), was superior over the proline series, in both the enzymatic and parasitic assays. They fulfill the hit criteria of the WHO[41] and were therefore chosen as starting point for further optimization. Moreover, the polar surface area (PSA), an important molecular descriptor for brain penetration,[42] and thus a criterion for targeting the second, neuroencephalitic stage of HAT, was significantly lower for the macrocyclic series than for the non-macrocyclic proline series (Figure S2). In conformational analyses of the macrocycles in the unbound state, the lowest-energy conformers showed an intramolecular H-bond,[43,44] which reduces the polar surface area by ~10 $Å^2$ compared to the bound state and thus contributes to their high trypanocidal activity (see Section S2 in the SI). The structures of the most potent hits **1** and **2** are shown in Figure 1. Although not particularly selective against hCatL, **1** displayed excellent selectivity towards the human cathepsins B (IC_{50} = 9000 nM), K (IC_{50} = > 25000 nM), S (IC_{50} = 2700 nM), and V (IC_{50} = 1043 nM).

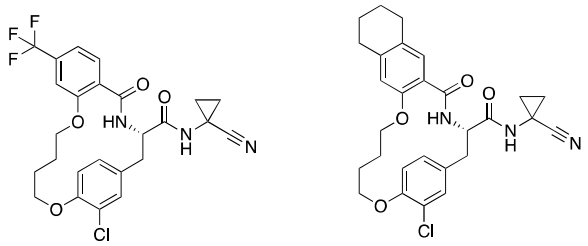

1
K_i (RD) = 11 nM
K_i (hCatL) = 10 nM
IC_{50} (*T. b. brucei*) 72h = 4 nM

2
K_i (RD) = 26 nM
K_i (hCatL) = 3 nM
IC_{50} (*T. b. brucei*) 72h = 1 nM

Figure 1. Structure of the two hits **1** and **2** and their binding affinities for RD and hCatL, respectively, as well as the cell-growth inhibition of *T. b. brucei*.

Motivated by these promising results, we were interested in further pursuing the optimization and evaluation of this macrocyclic ligand class as RD inhibitors against HAT.

Ligand Design. Two crystal structures of RD, released in 2009 and 2010 (PDB IDs: 2P7U[33] and 2P86[22]), respectively, and the co-crystal structures of related macrocycles with hCatL (see Section S7 in the SI) enabled the use of SBDD for further ligand optimization. Macrocycle **1** possesses a nitrile warhead, which is supposed to undergo reversible-covalent binding with the catalytic Cys25 at the active site of RD.[39] The formed thioimidate[45] is stabilized by the oxyanion hole of the protease, as seen in the modeled (with MOLOC,[46] MAB force field) binding mode of **1** in RD (protein coordinates taken from PDB ID: 2P7U[33], 1.65 Å resolution) (insert of Figure 2A). In analogy to the interactions in hCatL, the ligand forms hydrogen bonds to the backbone NH and C=O groups of Gly66 and Asp161, respectively, and fills the S2 and S3 pockets of RD, thereby establishing multiple lipophilic contacts with the enzyme (Figure 2B). There is high sequence conservation in the ligand binding site between RD and hCatL, however some amino acid differences become apparent in the S2 and S3 pockets (Figure 2B), which were targeted to improve the selectivity for RD. While this ligand class already contains many drug-like properties, modifications to increase the metabolic stability by changing the saturated macrocyclic bridge and by introducing amide isosters, were undertaken. Compounds **1**–**18** (Table S1), tested in the initial screen, featured salicylic acid derivatives addressing the S3 pocket of RD. In a first step, the introduction of extended S3 pocket vectors was initiated, to probe if these compounds will possess an increased selectivity against hCatL. In a second step, aromatic heterocycles were introduced into the S3 pocket vector and later also on the phenyl ring filling the S2 pocket.

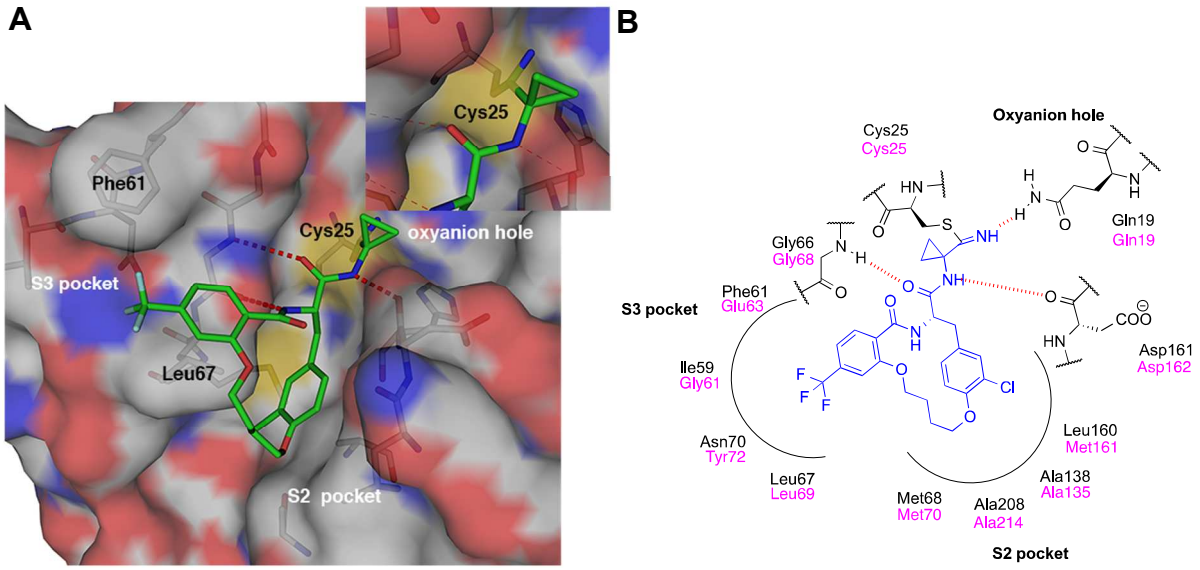

Figure 2. (**A**) Predicted binding mode of macrocycle **1** in complex with RD (protein coordinates taken from PDB ID: 2P7U[33], 1.65 Å resolution). Color code: gray C_{RD}, green C_{ligand}, red O, blue N, yellow S. Atomic surface shown. The insert shows the expected thioimidate formation by the catalytic Cys25. (**B**) Schematic binding mode of **1**, showing the putative covalent bond between Cys25 and the nitrile head group and the stabilization of the formed thioimidate by the oxyanion hole. The residues from RD are labeled in black and the residues from hCatL in magenta. Hydrogen bonds are represented as red dashed lines in (**A**) and (**B**).

SAR Exploration in the S3 Pocket of RD. *Synthesis.* The syntheses of macrocycles **1**, **2**, and **19a–e** relied on a convergent approach (Scheme 1). The amino building block **20** was prepared from commercially available *N*-[(*tert*-butoxycarbonyl]-3-(chloro)-L-tyrosine dicyclohexylammonium salt (**21**), which was doubly allylated to give **22** (Scheme 1a). Saponification of **22** yielded **23**, and amide coupling of **23** with 1-aminocyclopropylcarbonitrile hydrochloride in the presence of HATU and iPr_2NEt afforded Boc-protected **24** (not shown). *N*-Boc deprotection in neat formic acid, which avoided any decomposition or hydrolysis of the

nitrile, gave **20**. Similarly, salicylic acid derivatives **25a–f** were doubly allylated (**26a–f**) and saponified, yielding **27a–f** (Scheme 1b). Amide coupling between **20** and **27a–f** led to compounds **28a–e** (Scheme 1c). Ring-closing metathesis using either Grubbs catalyst 2nd generation[47] or Grubbs-Hoveyda[48] catalysts provided macrocycles **19a–e** featuring a *trans*-configured alkene as a mixture of atropisomers (see below). Reduction of the alkene in **19a,b** using H_2 and Pd/C 10% afforded macrocycles **1** and **2** in moderate yields, because of ring-opening of the macrocycles.[35]

Scheme 1. Synthesis of Macrocycles 1,[35] 2,[35] and 19a–e[a]

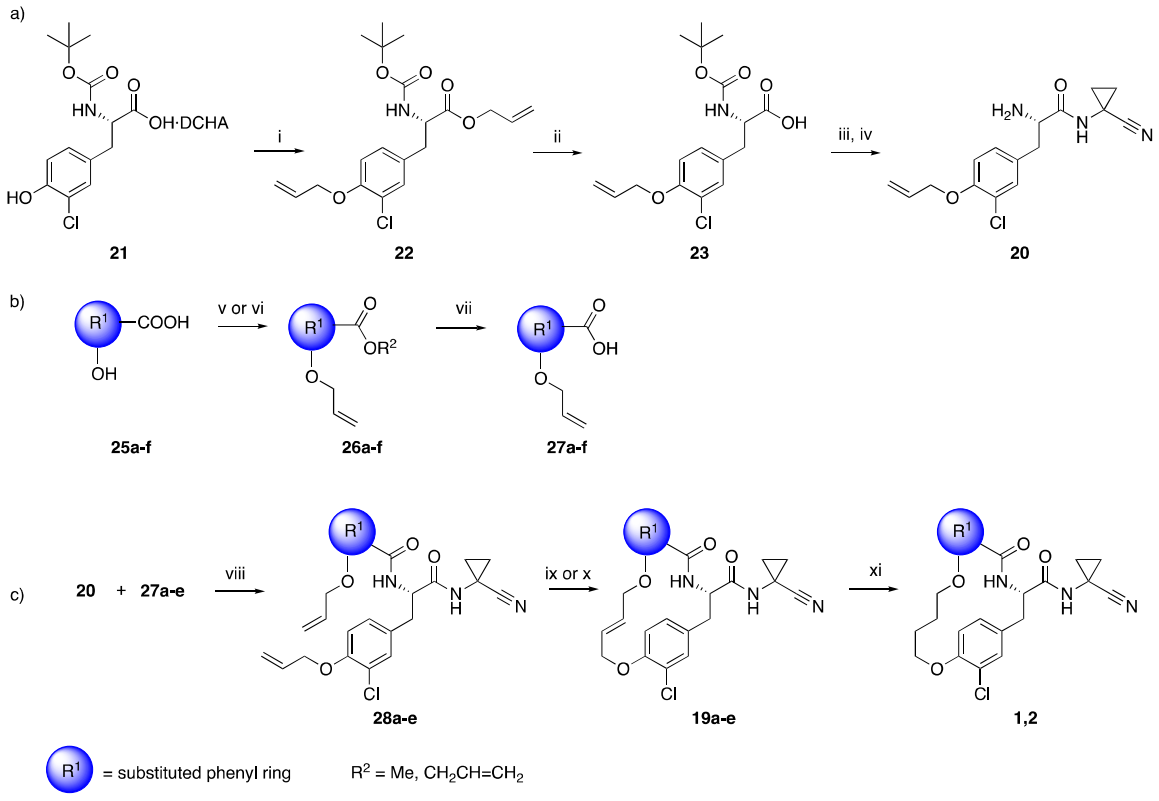

[a]Reagents and conditions: (i) allyl bromide, Cs_2CO_3, DMF, 16 h at 22 °C, 62%; (ii) LiOH, THF/H_2O/MeOH 2:2:1, 1 h at 22 °C, 100%; (iii) 1-aminocyclopropylcarbonitrile·HCl, HATU or TBTU, *i*Pr_2NEt, DMF or DMA, 4 h at 22 °C, 54%; (iv) HCOOH, 2 h at 22 °C, 100%; (v) allyl bromide, Cs_2CO_3, DMF, 16 h at 22 °C, 89–100%; (vi) allyl bromide, K_2CO_3, acetone, 16 h at 22 °C, 89–100%; (vii) LiOH, THF/H_2O/MeOH 2:2:1, 1 h at 22 °C, 19–99%; (viii) HATU, *i*Pr_2NEt, DMF, 2 h at 22 °C, 22–100%; (ix) Grubbs catalyst 2nd generation, CH_2Cl_2, 2 h at 50 °C; 43–53%; (x) Hoveyda-Grubbs 2nd generation catalyst, toluene, 2 h at 90 °C, 43–53%; (xi) H_2, Pd/C 10%, EtOAc, 4 h at 23 °C, 50–57%. The substituent R^1 represents the vector addressing the S3 pocket of RD and is defined in Table 1. DCHA = dicyclohexylamine; DMA = *N,N*-dimethylacetamide; DMF = *N,N*-dimethylformamide; HATU = 1-[bis(dimethylamino)methylene]-1*H*-1,2,3-triazolo[4,5-b]pyridinium 3-oxide hexafluorophosphate; TBTU = *O*-(Benzotriazol-1-yl)-*N,N,N′,N′*-tetramethyluronium tetrafluoroborate; THF = tetrahydrofuran.

In addition, macrocycle **8**[35] could be oxidized in the presence of 2 equivalents of *m*CPBA, giving **29** (Scheme 2).

Scheme 2. Derivatization of 29.[a]

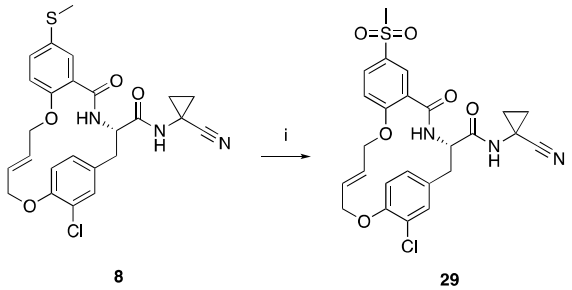

[a]Reaction conditions: (i) *m*CPBA (2 eq.), CH_2Cl_2, 20 min. at 0 °C, 36%. *m*CPBA = 3-chloroperbenzoic acid.

Enzyme Inhibition and Anti-parasitic Activities. The inhibition of RD and hCatL was quantified in a fluorometric assay, as previously reported (Table 1).[36–38] A selectivity index (SI) was defined as SI = K_i (hCatL)/K_i (RD). The cell-growth inhibition against *T. b. rhodesiense* was determined in the Alamar® blue assay[40] and the cytotoxicity evaluated by determining the cell-growth inhibition of rat myoblast L-6 cells. All macrocycles were inhibiting RD and hCatL in the

single to double-digit nanomolar K_i range. Macrocycle **19a** inhibited the cell-growth of *T. b. rhodesiense* with an IC_{50} of 4 nM, but increasing the size of the S3 substituent as in **19b–d** (Table 1) decreased the trypanocidal activity to the 300 nM IC_{50} range. Based on our structural models, the high potency of macrocycle **19e** (K_i (RD) = 1 nM, IC_{50} (*T. b. rhodesiense*) = 0.5 nM) might be accounted for by the parallel-displaced stacking interactions of the terminal ring of the naphthyl substituent with Phe61 ($d(C\cdots C_{Phe61})$ = 3.4 Å) (Figure S4 in the SI). Except for **19c** (IC_{50} (L-6) = 6.49 μM), low to moderate cytotoxicities (IC_{50} (L-6) > 35 μM) were observed in this series and the compounds possess excellent selectivities relative to L-6 cells.

Table 1. Inhibition of RD and hCatL, Selectivity Indices (SI), Cell-Growth Inhibition of *T. brucei rhodesiense*, and Cytotoxicity on L-6 cells of Selected Inhibitors.

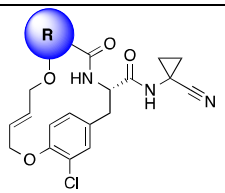

Compound	R =	K_i[a] (RD) [nM]	K_i[a] (hCatL) [nM]	SI[b]	IC_{50}[c] (*T. b. rhod.*) [μM] (SI[d])	IC_{50}[e] (L-6 cells) [μM]
19a	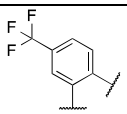	20.2	2.4	0.1	0.002 (18500)	37.0
19b	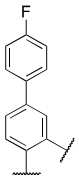	2.0	15.5	7.8	0.347 (131)	45.3

19c	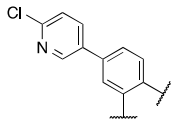	3.0	7.3	2.4	0.338 (19)	6.49
19d	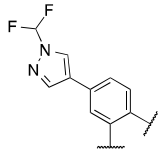	5.4	7.4	1.4	0.336 (132)	44.3
19e	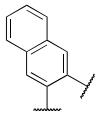	1.0	1.2	1.2	0.0005 (87600)	43.8
29	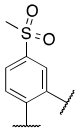	6.1	3.7	0.6	0.332 (n.a.[f])	>100

[a] Average of two measurements, each performed in duplicate; standard deviations < 10%; [b] SI = selectivity index = K_i (hCatL)/K_i (RD); [c] Average of at least 2 measurements, *T. b. rhodesiense* strain STIB 900, bloodstream form (trypomastigotes); standard deviations < 10%; [d] Selectivity index relative to the L-6 cells; [e] Average of at least 2 measurements, rat skeletal myoblast cell L-6 strain; standard deviations < 10%; [f] N.a. = not applicable.

SAR Exploration in the S2 Pocket of RD. *Synthesis.* Macrocycles **30a,d** and **31a–d** were derived from L-tyrosine **32**, which was iodinated to give **33** according to known procedures (Scheme 3).[49] Subsequent *N*-Boc protection (**34**, not shown) and bis-allylation with allyl bromide and Cs_2CO_3 afforded **35** in 78% yield, which was saponified with LiOH to give **36** in 94% yield. Amide coupling of **36** with 1-aminocyclopropanecarbonitrile hydrochloride gave **37** in 85%, and deprotection in neat HCOOH at 23 °C provided amine **38** in quantitative yield. A second amide coupling between **38** and carboxylic acids **27a** or **27f** afforded **39** and **40** in 33 and 70% yield, respectively. Ring-closing metathesis of **39** and **40** using Grubbs catalyst 2nd generation in CH_2Cl_2 at 50 °C gave the corresponding macrocycles **41** and **42** in 37 and 46% yield, respectively. All macrocycles isolated were shown to possess a *trans*-configured alkene. Reduction of the olefin with the commonly used Pd/C 10% and H_2 was initially attempted.

However, under these conditions, no hydrogenation was observed and instead de-iodination occurred. While treating **41** and **42** with Pt/C 10% and H_2 led to ring opening at both C_{sp2}–O positions, Raney-Nickel at 10 bars of H_2, 50 °C, overnight afforded **43** and **44** in 70 and 77% yield, respectively. Suzuki-Miyaura cross-coupling of **43** or **44** with potassium trifluoroborates afforded macrocycles **30a,d** and **31a–d** in 70–77% yield.[50] Reduction of the alkene functionality prior to further derivatization was crucial, as all attempted cross-couplings failed in its presence.

Scheme 3. Preparation of Macrocycles 30a,d and 31a–d[a]

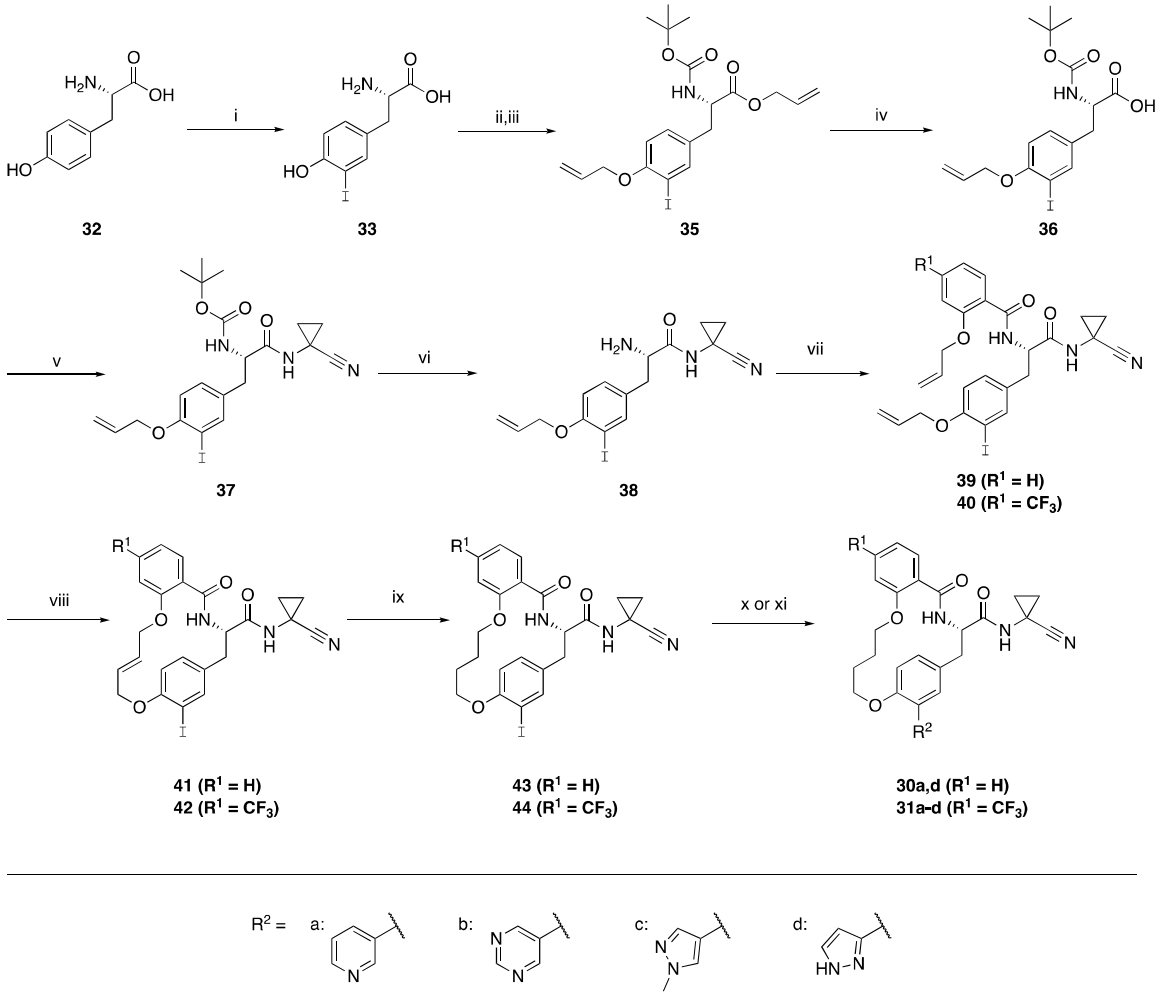

[a] Reaction conditions: (i) I_2, NH_4OH, 1 h at 22 °C, 33%; (ii) Boc_2O, Et_3N, H_2O/1,4-dioxane 1:1, 13 h at 22 °C, quant.; (iii) allyl bromide, Cs_2CO_3, DMF, 5 h at 22 °C, 78%; (iv) LiOH, THF/MeOH/H_2O 2:2:1, 1 h at 22 °C, 94%; (v) aminocyclopropylcarbonitrile hydrochloride, HATU, *i*Pr_2NEt, DMF, 3 h at 22 °C, 85%; (vi) HCOOH, 4 h at 22 °C, quant.; (vii) **27a** or **27f**, HATU, *i*Pr_2NEt, DMF, 2 h at 22 °C, 33–70%; (viii) Grubbs catalyst 2nd generation, CH_2Cl_2, 1 h at 50 °C, 37–46%; (ix) H_2, Ra-Ni, EtOAc, 20 h at 50 C and 10 bars, 70–77%; (x) R^2BF_3K, [$PdCl_2$(dppf)·CH_2Cl_2], Et_3N, Cs_2CO_3, 3:1:2 *i*PrOH/H_2O/CH_2Cl_2, 12 h at 90 °C, 13–85%; (xi) R^2BF_3K, [$Pd(OAc)_2$], RuPhos, Na_2CO_3, EtOH, 18 h at 85 °C, 13–85%. Dppf = 1,1'-bis(diphenylphosphanyl) ferrocene; RuPhos = 2-Dicyclohexylphosphino-2′,6′-diisopropoxybiphenyl.

Biological Results. Macrocycles **41–44** inhibited RD (K_i = 20–89 nM) efficiently, with however no selectivity against hCatL (K_i = 2.4–13.4 nM, SI = 0.1) (Table 2). The parasitic cell growth was inhibited in the sub- to single-digit nanomolar range (IC_{50} = 0.3–3 nM). Ligands **41–44** presented moderate cytotoxicity in the L-6 rat skeletal myoblast assay (IC_{50} = 37–56 μM). The presence of the trifluoromethyl group on the P3 substituent seems to consistently enhance the trypanocidal activity as was also observed for the comparison between **30a,d** and **31a–d**.

Introducing a 5- or 6-membered heterocycle at the 3-position of the L-tyrosine moiety as in **30a,d** and **31a–d** led to a substantial loss in binding affinity of 3–20-fold in RD and hCatL, which was reflected in the results of the cell-growth inhibition assays (IC_{50} (*T. b. rhodesiense*) = 0.03–3.88 μM). Some of the loss in affinity upon introduction of a 6-membered heterocycle at the 3-position of the L-tyrosine moiety may be rationalized by the fact that substantial ligand strain is generated to fit the ligand into the S2 pocket of RD (Figure 3). We note that some compounds potently inhibited trypanosome growth, despite having relatively poor affinity for RD, and tentatively assign this to off-target effects of the novel biaryl-type pharmacophore.

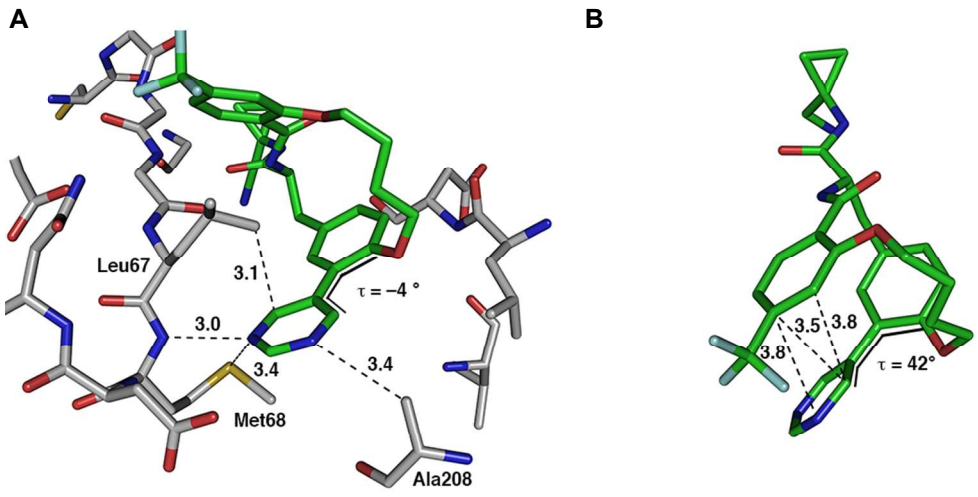

Figure 3. (**A**) Predicted binding mode of macrocycle **31b** in complex with RD (protein coordinates taken from PDB ID: 2P86[22], 1.16 Å resolution), highlighting the unfavorable torsion angle $\tau = -4$ ° in the bound state; (**B**) Macrocycle **31b** optimized in the free state, showing a probable hydrophobic collapse of the ligand in solution. The torsion angle $\tau = 42°$ in the unbound state is ideal for such biaryl systems.[51] Color code: green C_{ligand}, gray $C_{protein}$, red O, blue N, yellow S, cyan F. Distances given in Å.

Table 2. Inhibition of RD and hCatL, Selectivity Indices (SI), Cell-Growth Inhibition of *T. brucei rhodesiense*, and Cytotoxicity on L-6 cells of Selected Inhibitors.

Compound	R^1	R^2	K_i[a] (RD) [nM]	K_i[a] (hCatL) [nM]	SI[b]	IC_{50}[c] (*T. b. rhod.*) [μM] (SI[d])	IC_{50}[e] (L-6 cells) [μM]
		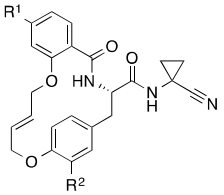					

41	H	I	2.5	n.d.[f]	n.d.	n.d.	n.d.
42	CF_3	I	8.7	5.6	0.6	0.3 (101)	30.15
		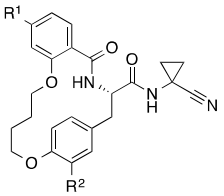					
43	H	I	n.d.	n.d.	n.d.	n.d.	n.d.
44	CF_3	I	57.4	5.8	0.1	0.03 (1892)	56.75
30a	H		837	997	1.2	1.93 (n.a.[g])	>100
31a	CF_3		751	824	1.1	0.018 (4011)	72.2
31b	CF_3		>20000	6393.3	n.d.	0.509 (n.a.[g])	>100
31c	CF_3	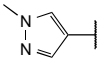	870	676	0.8	0.019 (n.a.[g])	>100
30d	H		1085.9	1105.7	1.0	1.23 (70)	86.5
31d	CF_3		45% inh. at 20 μM	1364.2	n.d.	0.14 (n.a.[g])	>100

[a] Average of two measurements, each performed in duplicate, standard deviations < 10%; [b] SI = selectivity index = K_i (hCatL)/K_i (RD); [c] Average of at least 2 measurements, *T. b. rhodesiense* strain STIB 900, bloodstream form (trypomastigotes), standard deviations < 10%; [d] Selectivity index relative to the L-6 cells; [e] Average of at least 2 measurements, rat skeletal myoblast cell L-6 strain, standard deviations < 10%; [f] n.d. = not determined; [g] n.a. = not applicable.

Atropisomerism and Racemization of Selected Macrocycles. Atropisomerism, *i.e.* the hindered rotation about single bonds leading to planar chirality,[52] is an often overlooked source

of stereoisomerism leading to the formation of diastereoisomers or enantiomers.[53–56] Discrete, stable atropisomers may feature greatly differing binding affinities as well as physico-chemical and ADME properties.[55]

Atropisomers have been classified by LaPlante *et al.* in three classes I–III, based on their half-lives of interconversion ($t_{1/2}$).[54] Class I atropisomers feature rapid rotation and short half-lives for isomerization ($\Delta G^{\ddagger}$ < 20 kcal mol^{-1}). In this case, atropisomerism is not relevant for the stereochemical integrity of a drug. Class II atropisomers have higher barriers to rotation ($\Delta G^{\ddagger}$ = 20–30 kcal mol^{-1}), and the half-lifes $t_{1/2}$ of the atropisomers are now in the range of minutes to several hours, relevant for the stereochemical integrity. It is therefore important for drug development to analyze Class II atropisomer interconversion in greater detail. Exposure to the active stereoisomer will be controlled by the interconversion rate.[56] Also, half-lives of the isomers can become longer than the half-lifes of their *in vivo* elimination, leading to *in vivo* enrichment of one isomer. A method used for detecting class II atropisomers is HPLC analysis on chiral supports, as exemplified by the determination of the racemization half-life of anthranilic acid HCV polymerase inhibitors.[56] Class III atropisomers ($\Delta G^{\ddagger}$ > 30 kcal mol^{-1}) have half-lifes $t_{1/2}$ of years, and the individual stereoisomers can be separated, isolated, and safely stored.

Most of the macrocycles reported herein possess planar chirality[52] and were isolated as 1:1 or 3:2 atropisomeric mixtures. We applied a method similar to the one reported by LaPlante *et al*[56] to determine the half-lives for isomerization of macrocycle **41** (Figure 4, Section S5 in the SI). The atropisomeric mixture of **41** was separated by HPLC on a chiral column (heptane/EtOH 7:3 for 20 min) at 22 °C. Upon injection on the column, two peaks were observed at a 57:43 ratio, corresponding to the (R_p,S) and (S_p,S) (where p = planar chiral) diastereoisomers (not assigned).

For the analysis, one peak (B) was collected, and re-injected on the same HPLC column (injection volume = 10 μL, flow rate = 1 mL min^{-1}) under the same conditions at various time points t = 5, 25, 45, 65, 90, and 200 min (Section S5 in the SI). After 200 min, integration of the peaks was performed at λ = 220 nm and the initial atropisomeric mixture was recovered.

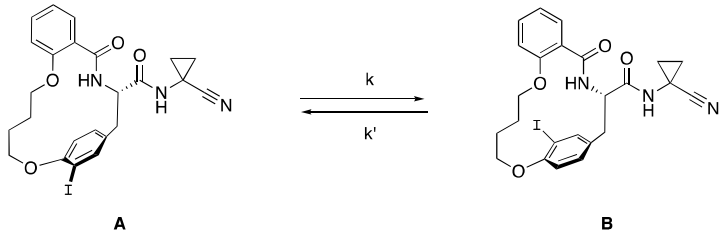

Figure 4. Slow equilibrium between the two diastereoisomeric atropisomers **A** and **B** of macrocycle **41**. The drawing of compound **A** depicts the (R_p,S) configuration and the drawing of **B** the (S_p,S) configuration, assigned according to the rules for planar chirality[52] but the configurations were not experimentally assigned. X-ray crystal structures later showed that the (S_p,S) diastereoisomer of the macrocycles is bound exclusively (see below).

A half-life for isomerization of $\tau_{1/2}$ = 37.5 min was extrapolated by curve-fitting (Figure S20 in the SI), suggesting that **41** lies within class II at 22 °C. However upon repeating the experiment at 37 °C, immediate re-equilibration was observed. Therefore, the exposure of macrocycle **41** should not be controlled by its interconversion half-life.

Structural Analysis in the Presence of RD. The binding mode of the macrocyclic ligands was determined for RD and hCatL by X-ray crystallography in order to better understand their molecular recognition pattern (Figures 5–6, Sections S6 (RD) and S7 (hCatL) in the SI). Three crystal structures of ligands **1**, **3**[35], and **7**[35] in complex with RD were obtained (**1**: PDB ID:

6EX8, 1.6 Å resolution; **7**[35]: PDB ID: 6EXO, 1.9 Å resolution, and **3**[35]: PDB ID: 6EXQ, 2.5 Å resolution, ligand structures are shown in Figure 5D).

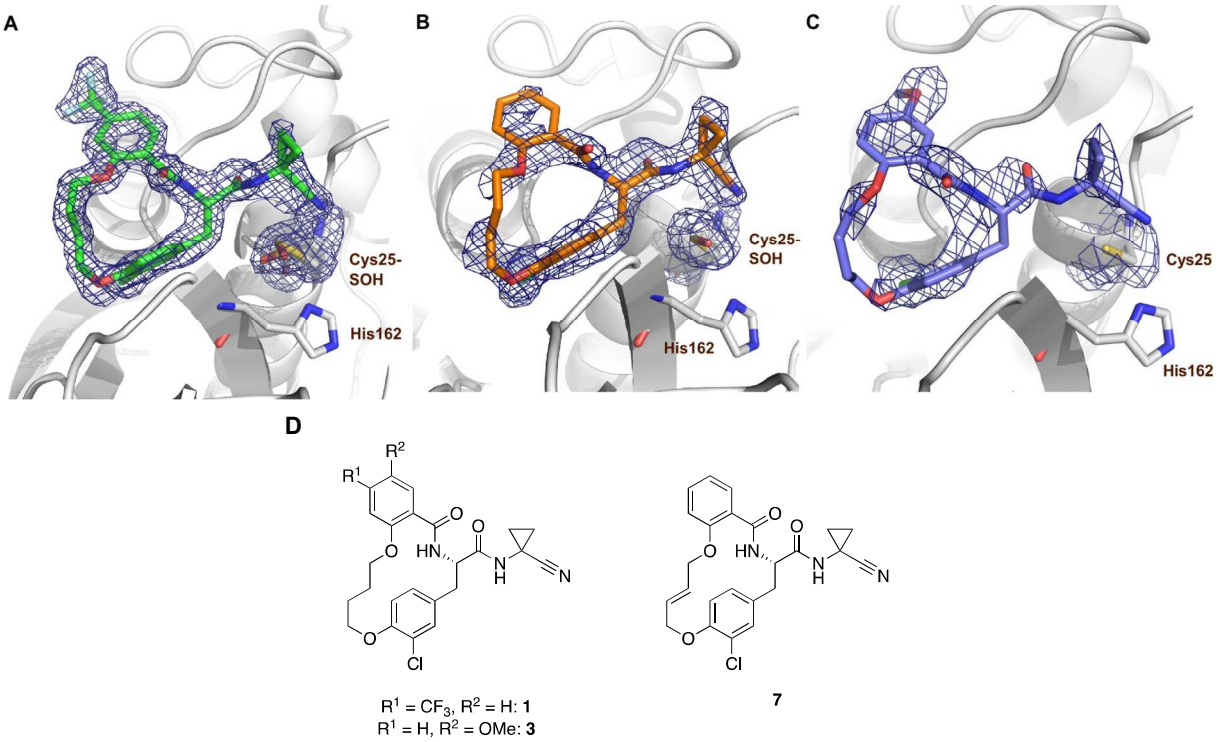

Figure 5. (**A**) F_o-F_c Electron density map shown as a blue mesh of ligand **1** and the active site cysteine of RD (PDB ID: 6EX8, 1.6 Å resolution). The enzyme is shown in gray and ligand **1** is shown in green. (**B**) Electron density map of ligand **7** and the active site cysteine of RD (PDB ID: 6EXO, 1.9 Å resolution), the color code is the same as in **A**, ligand **7** is shown in orange; (**C**) Electron density map of ligand **3** and the active site cysteine of RD (PDB ID: 6EXQ, 2.5 Å resolution), the color code was maintained, and ligand **3** is shown in violet; (**D**) Chemical structures of ligands **1**, **3**, and **7**. The F_o-F_c maps were calculated in the absence of the inhibitor and the active site cysteine and are contoured at 2.5 σ. Refinement for Cys25-SOH in (**A**) was carried out in two different orientations at 50% occupancy each. In (**C**), the oxidation of Cys25 is

not visible due to the lower resolution of the dataset but can be assumed because of the same crystallization conditions for all three structures.

The crystal structure of ligand **1** bound to RD at 1.6 Å resolution is discussed here in more detail (PDB ID: 6EX8, Figure 6A). The complex crystallized in space group P1, with two chains of mature enzyme in the asymmetric unit. The observed binding mode of ligand **1** is in accordance with our design (Figure 2). In all three crystal structures, the (S_p,S)-configured atropisomer binds exclusively to the protein. However, to our surprise, the nitrile warhead, which was systematically covalently bound to the nucleophilic Cys25 in the hCatL complexes with proline-based inhibitors,[39] triazine nitriles,[38,57] and dipeptidyl nitriles,[58] did not form a covalent bond with Cys25 (Figure 6A). Instead, Cys25 was oxidized to a sulfenic acid (Cys25-SOH), which is most likely due to the extended time until crystals formed.[59] In complex **1**, the C≡N lies at a distance of d(N≡C···S) = 3.3 Å from the Cys25-SOH. This nitrile is further stabilized by a N···HN_{Gln19} contact (d(N···HN_{Gln19}) = 3.3 Å) with the side chain of Gln19 being in the oxyanion hole. Our enzyme kinetics studies showed that the inhibitors bind in a reversible-covalent manner.[37,38] It is possible, that the inhibitors formed a covalent bond and reverted over time to the non-covalent state prior to crystallization, together with the oxidation of Cys25, which is also reversible.[60]

The S2 pocket is filled with the aromatic ring of the 3-chloro-L-tyrosine moiety, which is sandwiched between Leu67 and Leu160 and undergoes C–H···π interactions with Leu67 (d(C_{Leu67}···C) = 3.6 Å) and Leu160 (d(C_{Leu160}···C) = 3.9 Å). The chloro substituent is in the vicinity of Met68 (d(Cl···S_{Met68}) = 4.1 Å) and forms a short contact to the terminal methyl group of Met68 (d(Cl···C_{Met68}) = 3.6 Å) (contacts not shown). In the S3 pocket of RD, the trifluorophenyl ring lies on top of the Gly66–Leu67 amide bond plane at the entrance of the

pocket, with an interplanar angle of ~45º (d(C···C=O_{Gly66}) = 3.7 Å). The fluorine atoms of the trifluoromethyl group display short, potentially favorable contact distances with the phenyl ring of Phe61 (d(C_{Phe61}···F) = 3.5 Å), and the backbone NH of Asn70 (d(N_{Asn70}···F) = 3.2 Å). At d(C=O_{Asp60}···F) = 4.2 Å, the third F-atom avoids repulsive interactions with the side chain carboxylate of Asp60 (not shown). An overlay of the structures of macrocycle **7** in RD (PDB ID: 6EXO) and hCatL (PDB ID: 6EZP) shows two similar binding modes despite the fact that **7** binds covalently to hCatL and not to RD (Figure 6B). All three macrocycles bind in a similar way to RD, as shown by the overlay of the three co-crystal structures (Figure 6C). An additional X-ray structure of **14** bound to hCatL (PDB ID: 6F06) reveals as well a binding mode of **14** in a non-covalent fashion (Figure S24). In this case, the sulfur atom of Cys25 forms a complex with a Zn^{2+} ion together with a Cl^{-} ion and His162 making the sulfur atom unavailable for thioimidate formation.

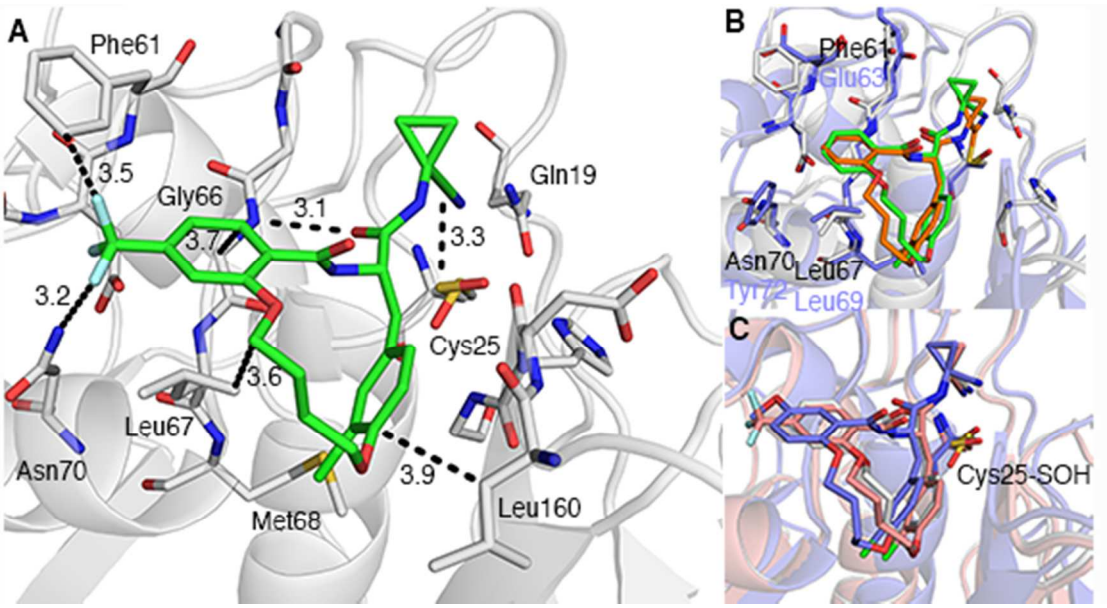

Figure 6. (**A**) Binding mode of **1** in complex with RD (PDB ID: 6EX8, 1.6 Å resolution), color code: green C_{ligand}, gray C_{enzyme}; (**B**) Overlay of the crystal structures of **7** in complex with RD (PDB ID: 6EXO, 1.9 Å resolution) and with hCatL (PDB ID: 6EZP, 2.34 Å resolution), color code: green $C_{ligand,RD}$, orange $C_{ligand,hCatL}$, gray C_{RD}, violet C_{hCatL}; (**C**) Overlay of all three crystal structures of macrocycles **1** (in pink, PDB ID: 6EX8, 1.6 Å resolution), **7** (in gray, PDB ID: 6EXO, 1.9 Å resolution) and **3** (in violet, PDB ID: 6EXQ, 2.5 Å resolution). Common color code: red O, blue N, yellow S. Distances given in Å and represented as dashed black lines.

Drug Metabolism and Pharmacokinetics. Macrocycle **1** features reasonable solubility at pH 6.5, and a log$D_{7.4}$ value of 3.7 was determined (Table 3). In addition, **1** did not inhibit the major cytochromes P450 significantly (IC_{50} (3A4) = 43 μM, IC_{50} (2D6) = 11 μM, IC_{50} (2C9) = 16 μM).

Table 3. *In Vitro* Data of 1.

LYSA[a] [μg/mL]	log$D_{7.4}$[b]	PAMPA[c] P_{eff}	IC_{50} [μM] CYPs 3A4; 2D6; 2C9
12	3.7	4	43/11/16

[a] Solubility determined by lyophilisation solubility assays (LYSA) at pH 6.5; [b] log$D_{7.4}$ = intrinsic distribution coefficient between octanol and aqueous buffer (pH 7.4), measured in a CAMDIS© assay; [c] Membrane permeability [nm s^{-1}] derived from the PAMPA assay.

The PK profile of **1** was characterized in mice, following intravenous administration (Table 4).

Table 4. Mouse Pharmacokinetic Profile of 1.

CL (mL min^{-1} kg^{-1})[a]	*Vss*[b] [L kg^{-1}]	$t_{1/2}$ [h][c]	B/P[d]
79	7.2	2.7	< 0.5

[a] Clearance; [b] Volume of distribution; [c] Half-life of compound in blood; [d] Brain-over-plasma ratio, parameters calculated by non-compartmental analysis of plasma concentration-time profiles.

Metabolic Stability Studies. Macrocycles **1** and **7** at 2 μM concentration in DMSO were incubated for 7 min in human and rat liver microsomes (see Section S9 in the SI). More than 98% of the parent compound **7** disappeared after the 7 min incubation. The results of mass spectrometry experiments showed that the linker was a site of metabolism and was readily oxidized ([*M* + 16] and [*M* + 32]) (Section S9). Thus, the modification of this linker, aiming at removing at least one of the ether bridges, was undertaken.

Linker Modification. *Synthesis.* Initial efforts to stabilize the linker focused on fluorinating at different positions, however all remained unsuccessful (see Section S10 in the SI). Using a similar synthetic strategy to the one depicted in Scheme 1, at least one of the ether bridges could be removed (Schemes 4 and 5). *N*-Alkylation of pyrazole derivatives **45a–d** with 4-bromobut-1-ene gave **46a–f**. Subsequent saponification provided carboxylic acids **47a–f**, which were coupled with **20** to give **48a–f**. Ring-closing metathesis afforded macrocycles **49a–f**.

Scheme 4. Preparation of Ligands 49a–d Described in Table 5.

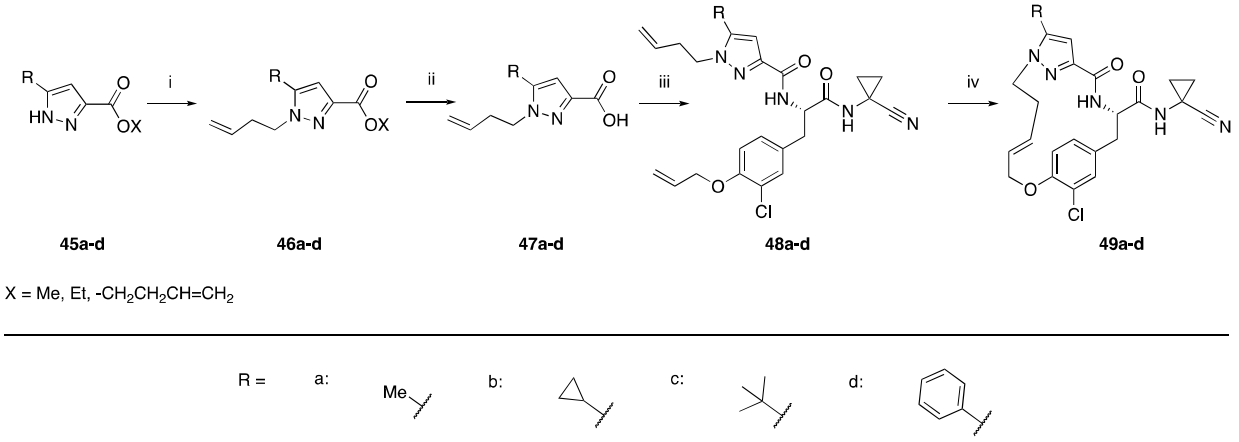

[a]Reaction conditions: (i) 4-bromobut-1-ene, Cs_2CO_3, DMF, 22 °C, 34–82%; (ii) LiOH, THF/H_2O/MeOH 2:2:1, 1 h at 22 °C, 100%; (iii) **20**, HATU, *i*Pr_2NEt, DMF, 22 °C, 21–67%; (iv) Hoveyda-Grubbs 2nd generation catalyst, toluene, 2 h at 90 °C, 16–22%.

Similarly, *N*-Alkylation of pyridone derivatives **50a,b** with 4-bromobut-1-ene gave **51a,b**. Subsequent saponification provided carboxylic acids **52a,b**, which were coupled with **20** to give **53a,b**. Ring-closing metathesis afforded macrocycles **54a,b** (Scheme 5).

Scheme 5. Preparation of Ligands 54a,b Described in Table 5.

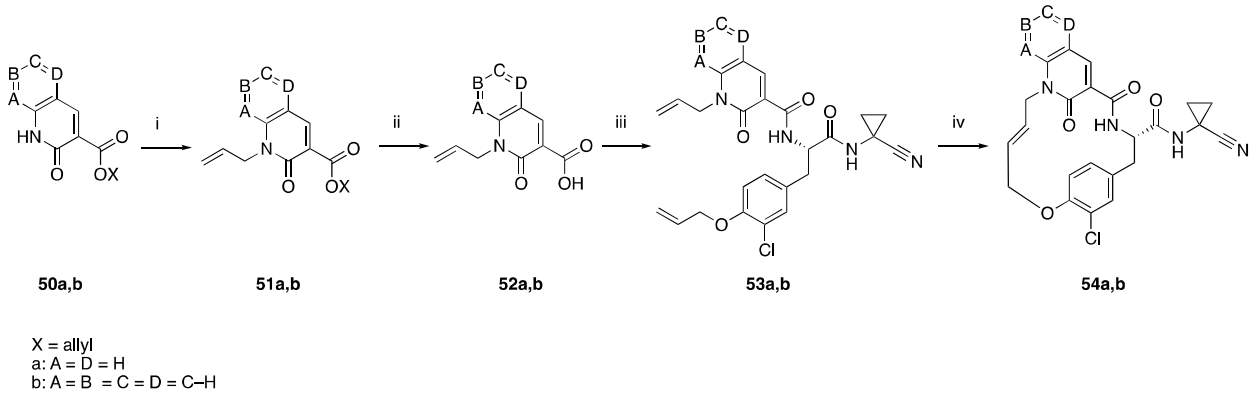

[a]Reaction conditions: (i) allyl bromide, Cs_2CO_3, DMF, 22 °C, 72–100%; (ii) LiOH, THF/H_2O/MeOH 2:2:1, 1 h at 22 °C, 100%; (iii) **20**, HATU, *i*Pr_2NEt, DMF, 22 °C, 65–67%; (iv) Hoveyda-Grubbs 2nd generation catalyst, toluene, 2 h at 90 °C, 12–26%.

In addition, treatment of **8**[35] with 3 equivalents of *m*CPBA afforded epoxide **55** as a 3:2 mixture of atropisomers (Scheme 6). The diastereoselectivity of the epoxidation was tentatively assigned considering the conformational restriction of the alkene and by 2D NMR.

Scheme 6. Derivatization of 8[35].[a]

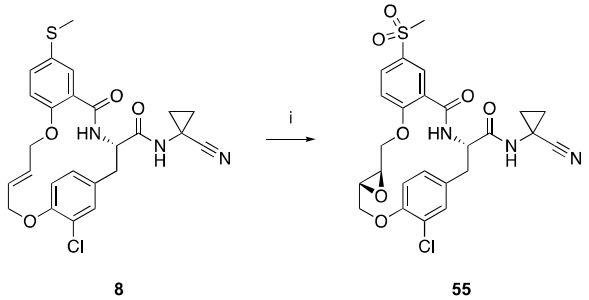

[a]Reaction conditions: (i) *m*CPBA (3 eq.), CH_2Cl_2, 55%.

Although alkyne metathesis[61] remained unsuccessful, an alkyne bridge could be introduced to yield macrocycles **56a** and **56b** (Scheme 7). Protection of salicylic acid derivative **57** gave **58**, which was *O*-alkylated with 1,4-dibromobut-2-yne to afford **59**. *N*-Boc-protected 3-chloro-L-tyrosine (**21**) was methylated to give **60**, which was *O*-alkylated with **59** to provide **61**. Saponification of **61** (giving **62**, not shown) and subsequent amide coupling with 1-aminocyclopropylcarbonitrile hydrochloride yielded **63**. Deprotection in neat formic acid yielded **64**, which was cyclized to yield atropisomers **56a** and **56b**. The structure of **56a** was assigned by 2D NMR.

Scheme 7. Preparation of 56a and 56b[a]

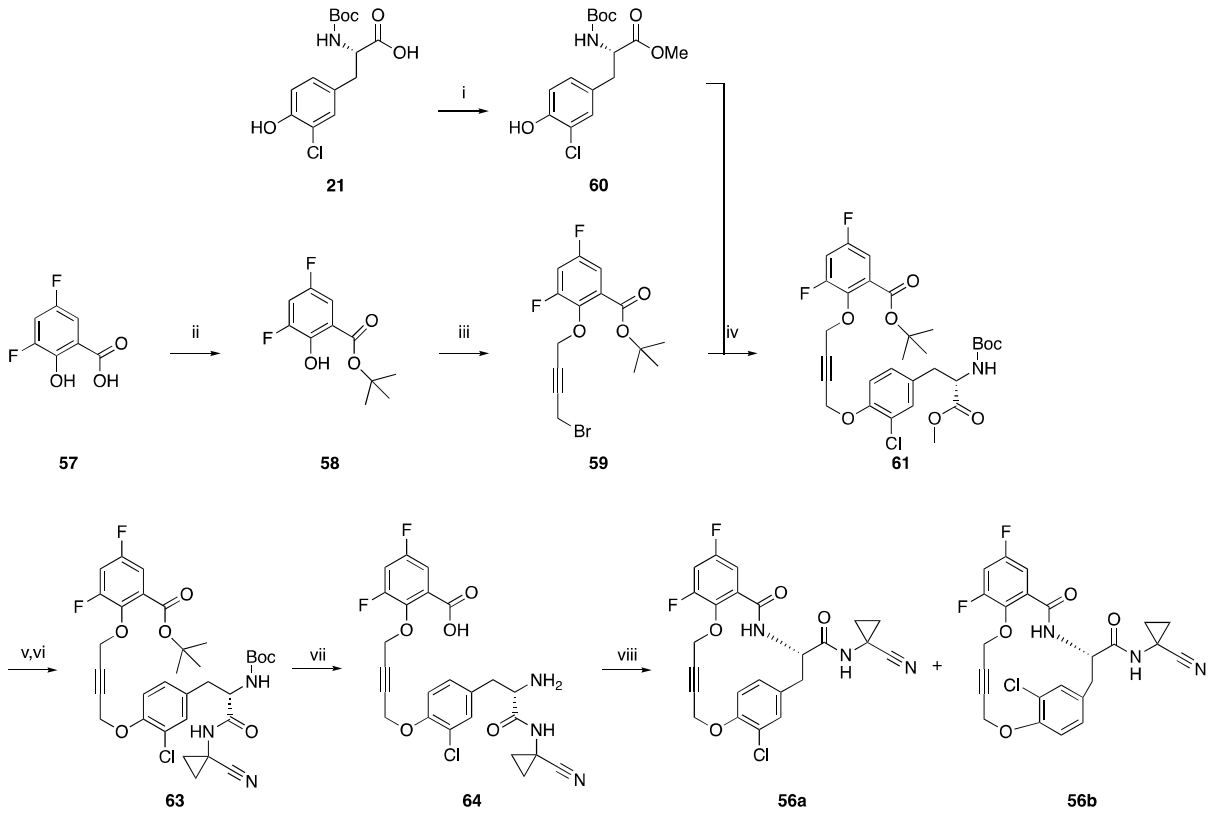

[a]Reaction conditions: (i) methylation; (ii) 1. CDI, DMF, 2 h at 40 °C; 2. DBU, *tert*-BuOH, DMF, 14 h at 40 °C, 86%; (iii) 1,4-dibromobut-2-yne, K_2CO_3, KI, acetone, 23 °C, 77%; (iv) K_2CO_3, KI, acetone, 23 °C, 59%; (v) LiOH, 2:1 THF/H_2O, 23 °C; (vi) aminocyclopropylcarbonitrile hydrochloride, HATU, CH_2Cl_2/DMF, 23 °C, 70%; (vii) HCOOH, 23 °C (viii) HATU, CH_2Cl_2, 23 °C, 68%. CDI = 1,1'-carbonyldiimidazole; DBU = 2,3,4,6,7,8,9,10-octahydropyrimido[1,2-a]azepine.

Enzyme Inhibition and Anti-parasitic Assays. The pyrazole series **54a,b** led to potent inhibitors of RD and hCatL and inhibited the cell-growth of *T. b. rhodesiense* in the nanomolar IC_{50} range (Table 5). Although no general selectivity was achieved with these compounds, **49d** showed a 10-fold selectivity for RD, which is the best measured for the entire macrocyclic ligand class. Pyridone derivative **54a** led to a decrease in binding affinity and cell-growth inhibition, however **54b** was potent in the cell-based assay for which a good explanation is not yet available. Introducing an epoxide onto the bridge as in **55** significantly reduced the trypanocidal activities.

On the other hand, compounds **56a,b** with an alkyne linker were similarly potent to macrocycles **1** or **2**. These compounds (except epoxide **55a**) led to highly selective compounds for *T. b. rhodesiense* relative to L-6 cells.

Table 5. Inhibition of RD and hCatL, Selectivity Indices (SI), Growth Inhibition of *T. b. rhodesiense*, and Cytotoxicity on L-6 Cells of Inhibitors 49a–d, 54a,b, 55, and 56a,b.

Compound	Structure	K_i[a] (RD) [nM]	K_i[a] (hCatL) [nM]	SI[b]	IC_{50}[c] (*T. b. rhod.*) [μM] (SI[d])	IC_{50}[e] (L-6) [μM]
49a	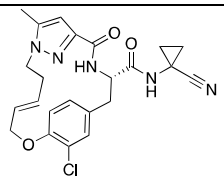	52.4	40.3	0.8	0.006 (n.a.)	>100
49b	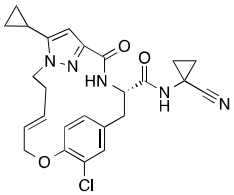	17.2	2.5	0.1	0.005 (12120)	60.6
49c	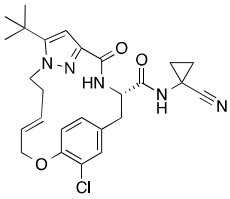	18	2.3	0.1	0.0006 (64167)	38.5
49d	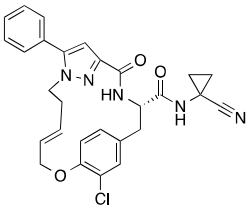	5.2	55.7	11	0.0006 (66667)	40.0

54a	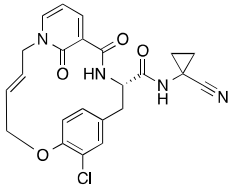	> 20 μM	> 20 μM	n.a.[f]	47.8 (n.a.)	>100
54b	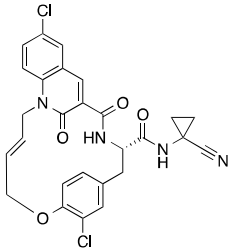	299.0	273.5	0.9	0.008 (2025)	16.2
55	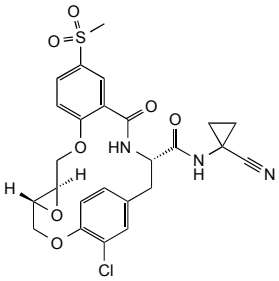	135.1	4.6	0.03	16.9 (5)	84.7
56a	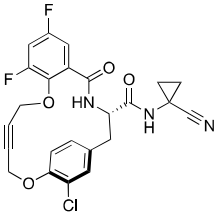	80.6	24.1	0.3	0.008 (5700)	45.6
56b	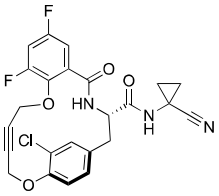	4.8	1.2	0.3	0.004 (11775)	47.1

[a] Average of two measurements, each performed in duplicate, standard deviations < 10%; [b] SI = selectivity index = K_i (hCatL)/K_i (RD); [c] Average of at least 2 measurements, *T. b. rhodesiense* strain STIB 900, bloodstream form (trypomastigotes), standard deviations < 10%; [d] Selectivity index relative to the L-6 cells; [e] Average of at least 2 measurements, rat skeletal myoblast cell L-6 strain, standard deviations < 10%; [f] N.a. = not applicable.

Selectivity of the Macrocycles Against Other Parasites. The *in vitro* cell-growth inhibitions of selected macrocycles were determined for a panel of other protozoan parasites consisting of *T. cruzi*, *Leishmania donovani*, and *Plasmodium falciparum* (Section S11 in the SI), the causative

agents of Chagas' disease, leishmaniasis, and malaria tropica, respectively. The inhibition by the corresponding typical antiprotozoal drugs is reported for comparison. All compounds presented good to excellent selectivity against the other parasites, suggesting that our inhibitors selectively target RD, despite the structural similarities to the parasitic enzymes cruzain[62] (from *T. cruzi*), the leishmanial cysteine proteases,[63] and falcipain-2[36] (from *P. falciparum*). In addition, they all possess moderate to low cytotoxicity, as demonstrated by the IC_{50} values against L-6 rat myoblast cells.

P-gp Efflux Ratio and Brain Penetration. In order to be effective in stage 2 HAT, a drug needs to be able to cross the blood brain barrier (BBB).[34] One of the parameters used to evaluate brain penetration is the P-glycoprotein (P-gp) efflux ratio (ER), which inversely correlates with brain penetration for cell-permeable compounds.[42,64] The human and mouse ER were determined for macrocycles **1** and **2** in a transwell assay using P-gp (MDR1) overexpressing LLCPK1 cells (Table 6). Both macrocycles present a high P-gp liability, with an ER in human of 26. With two amide bonds and a nitrile in their structure, **1** and **2** are good P-gp substrates, despite the putative intramolecular H-bond that should engage at least one of these amides. The PSAs (see Section S2 in the SI for a full discussion) of **1** (80.2 $Å^2$) and **2** (78.2 $Å^2$) are however well within the ideal range for CNS penetration (40 $Å^2$ < PSA < 90 $Å^2$).[42]

Table 6. P-Glycoprotein (P-gp) Efflux Ratio (ER) and Calculated PSA of Selected Inhibitors.

Cpd	P-gp ER (human)[a]	P-gp ER (mouse)	PSA [Å^2][b]
1	26	53	80.2
2	26	38	78.2

[a] ER in LLCPK1 cells stably expressing human MDR1; [b] PSA calculated using the MOLOC companion program Msrfvl based on a low-energy conformation generated with the MOLOC program Mol3d.

Nevertheless, brain penetration was evaluated in rats (Table 7), which were treated with an infusion of 3 mg kg^{-1} of **1** over the course of 30 min. The animals were then sacrificed, and plasma, brain, and cerebro-spinal fluid (CSF) concentrations were determined. Reasonable brain penetration was observed, despite the P-gp ER of 53 in mice. The free brain concentration, substituted by CSF concentrations, remains rather low.

Table 7. Brain Penetration of Ligand 1 In Rats.

Plasma conc. [ng/mL][a]	Brain conc. [ng/g][a]	CSF conc. [ng/mL][a]	Brain/Plasma ratio[a]	CSF/Plasma ratio[a]
404	256	2.3	0.7	0.006

[a] Average of three independent measurements.

Amide Isosters to Reduce P-gp Affinity. To decrease the P-gp ER and in turn increase the brain penetration, the removal of one amide was undertaken by introducing an amide isoster.

Replacement of an amide by a *β,β,β*–trifluoroethylamine group has been reported to increase the bioavailability of odanacatib, a cathepsin K inhibitor.[65]

Synthesis. Macrocycle **65** was prepared starting from phenol **66**, which was alkylated with 3-bromoprop-1-ene to give **67** (Scheme 8). Reductive amination with $NaCNBH_3$ of **67** with **68**, (prepared from **22**), preceded by activation with $TiCl_4$, yielded the secondary amine **69**. Saponification of **69** gave **70** (not shown**)** on which the aminocyclopropylcarbonitrile warhead was coupled with HATU and Hünig base to afford **71**. Macrocyclization of **71** using Grubbs catalyst 2nd generation gave **65**, which was isolated as a diastereoisomeric mixture.

Scheme 8. Preparation of Macrocycle 65.[a]

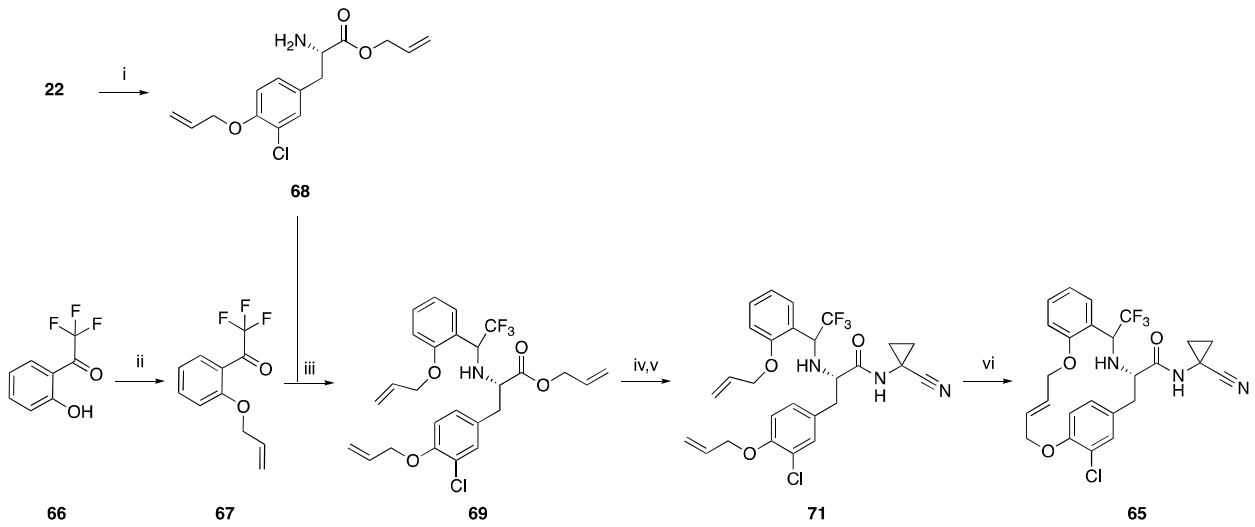

[a] Reaction conditions: (i) 1. CS_2CO_3, 5 min at 23 °C; 2. 3-bromoprop-1-ene, DMF, 23 °C, xx%; (ii) 1. $TiCl_4$ (1M in CH_2Cl_2), *i*Pr_2NEt, CH_2Cl_2, 22 h at 23 °C; 2. $NaCNBH_3$ in MeOH, 30 min at 23 °C; 45%; (iii) LiOH, 2:1:1 THF/H_2O/MeOH, 23 °C; 33%; (iv) aminocyclopropylcarbonitrile, *i*Pr_2NEt, HATU, DMF, 23 °C, 58%; (v) Grubbs catalyst 2nd generation, CH_2Cl_2, 50 °C, 31%.

Enzyme Inhibition and Anti-parasitic Assays. Introducing an amide isoster in the macrocyclic scaffold as in **65** led to a decrease in potency against RD (K_i = 258 nM) and hCatL (K_i = 443

nM). The cell-growth inhibition of *T. b. rhodesiense* even shifted to the micromolar range (IC_{50} = 9.5 μM), suggesting that this particular amide is crucial for trypanocidal activity, and the development of such scaffolds was not further pursued. The cytotoxicity of the macrocycle on the rat skeletal myoblast L-6 cell strain was moderate (IC_{50} = 31.7 μM)).

Reversibility of Drug Effects. The antiparasitic activity of selected macrocycles was assessed in experimental models of HAT. *In vitro*, they exhibited parasite growth inhibition activity against *T. b. rhodesiense* (STIB900), with good dose-response relations when assessed in the standard 72 h assay[66] (Section S13 in the SI). Compounds **1**, **10**, **19a**, and **49b** exhibited an irreversible drug effect in pulse incubation assays with 24 h and 48 h drug pressure, followed by a 72 h recovery period. The best trypanocidal activity in the pulse incubation assays was shown by compound **1** with an IC_{50} value of 0.01 μM.

***In Vivo* Activities.** Motivated by the promising *in vitro* results, we tested macrocycles **1** and **8** in *T. b. rhodesiense* acute model of infection at intraperitoneal (i.p.) doses of 25 mg kg^{-1} twice a day, for 4 days. While no improvement by comparison with the control was observed with macrocycle **8**, compound **1** was active with a parasitaemia reduction below detection level 24 h after the last treatment, with a relapse on day 10.25 and an extended survival (16.3 days) compared with the untreated control group (13 days). The exposure of macrocycles **1** and **8** (Table 8) indicates that the blood concentration decreases significantly after 4 hours, which may explain the relapse observed after 10.25 days for **1**.

Table 8. Blood Concentrations of Macrocycles 1 and 8, dosed on day 4 25mg/kg i.p. twice daily.

	Blood Concentration [ng/mL][a] at time past dose (hrs)		
Compound	**1 hr**	**4 hrs**	**16 hrs**
1	237 (119)	15.1 (4.2)	4.8 (0.6)
8	951 (86)	66.4 (9.6)	<10

[a] Average of four measurements (standard deviations).

CONCLUSION

Motivated by the structural similarities of hCatL and RD within their active sites, an hCatL inhibitor library provided by F. Hoffmann-La Roche Ltd. was screened against the enzyme rhodesain, a protein produced by *T. b. rhodesiense*, one of the causative agents of HAT. A series of macrocyclic lactams were identified as potent hits, with K_i (RD) < 500 nM, and five of these hits showed IC_{50} values (*T. b. brucei*) < 10 nM. One of these hits was used as a start for ligand design, and SARs addressing the S2 and S3 pockets of rhodesain were performed. The atropisomerism of one of the planar-chiral macrocycles was studied, showing an isomerization half-life ($t_{1/2}$) of 37.2 min at 23 °C. The binding mode of this ligand class was confirmed by three crystal structures in complex with RD (PDB IDs: 6EX8, 6EXO, and 6EXQ) and in hCatL (PDB IDs: 6EZP, 6EZX, and 6F06). Whereas the hCatL structures featured the expected covalent binding to the catalytic Cys, this Cys (Cys25) in RD was oxidized during the lengthy crystallization period to a sulfenic acid (Cys–SOH), which points towards a covalent-reversible reaction or to a non-covalent binding of the ligands. We assume, however, that the thioimidate is established during the various activity assays. The crystal structures showed only minor changes in the overall positioning of the ligand in the active site of RD.

Following metabolic stability studies, which highlighted the macrocyclic bridge as main site of metabolism, modifications of this linker were performed, leading to potent (K_i < 5 nM) and trypanocidal (IC_{50} (*T. b. rhodesiense*) < 10 nM) pyrazole derivatives **49a–d**. To evaluate the ability of the macrocyclic ligand class to cross the blood-brain barrier, the P-gp ER and the *in vivo* brain penetration were measured. Although encouraging, the results were not completely satisfying and a macrocycle containing an amide isoster was prepared, with the aim of reducing the ER. At last, the *in vivo* efficacy was evaluated for selected macrocycles. These compounds prevented the relapse of trypanosomes up to 10.25 days, and led to survival of the treated mice up to 16.25 days over controls.

EXPERIMENTAL SECTION

Determination of RD and hCatL Activity. The inhibitory constants (K_i) of the ligands against RD and hCatL were calculated using the Cheng-Prusoff equation[67] from the IC_{50} determined in a fluorescence-based assay, as previously described.[37,38]

***In Vitro* Evaluation.** The *in vitro* activities against *T. b. brucei*, *T. b. rhodesiense*, *T. cruzi*, *L. donovani* and *P. falciparum* as well as the cytotoxicity assessment in L6 cells were determined as reported elsewhere.[66,68] The following strains and parasite forms were used: *T. b. rhodesiense*, STIB900, trypomastigotes; *T. cruzi*, Tulahuen C2C4 (LacZ), amastigotes; *L. donovani*, MHOM-ET-67/L82, axenically grown amastigotes, *P. falciparum*, NF54, erythrocytic forms; and L6 cells, rat skeletal myoblasts.

log*D* Determination. Distribution coefficients were determined in a CAMDIS© (CArrier Mediated DIstribution System, EP2005102211A) assay, as previously reported.[69]

Membrane Permeability Determination. The permeability was determined *via* PAMPA (Parallel Artificial Membrane Permeation Assay), as previously reported.[70]

Solubility. The solubility was determined in a lyophilisation solubility assay (LYSA), as previously reported.[71]

Stability in Mouse Microsomes. The stability was determined in a NADH-dependent assay as previously reported.[71]

CYP Inhibition. The inhibition of the cytochromes P450 (CYP) 2C9, 2D6, and 3A4 was assessed using human liver microsomes and CYP-selective substrate metabolism reactions, as previously described.[72]

Mouse PK. All studies were conducted with the approval of the local veterinary authority in strict adherence to the Swiss federal regulations on animal protection and to the rules of the

Association for Assessment and Accreditation of Laboratory Animal Care International (AAALAC). Male adult C57BL/6J mice (Janvier Labs, France) were administered the test compounds intravenously (bolus). Test compounds were dissolved in *N*-methylpyrrolidinone and 40% (v/v) aqueous hydroxypropyl-γ-cyclodextrine (30/70 v/v) for intravenous (i.v.) administration. Blood was collected into K_2EDTA coated polypropylene tubes at 5 min, 15 min, 30 min, 1 h, 2 h, 4 h, and 8 h post dose sublingually or terminally by cardiac puncture under deep anesthesia with 5% isoflurane in pure oxygen. Blood was stored on ice and plasma was prepared within 30 min by centrifugation at 3000 × g for 5 min at 4 °C and frozen immediately. All plasma samples were stored at −20 °C. Compound concentrations in plasma from pharmacokinetic and pharmacodynamic studies were determined by means of liquid chromatography coupled to mass spectrometry (LC–MS/MS). Pharmacokinetic parameters were calculated by non-compartmental analysis using an in-house built software package.

MDR1-Mediated Transport. Porcine kidney epithelial LLC-PK1 cells stably transfected with Abcb1a (Mdr1a, mouse P-gp) or ABCB1 (MDR1, human P-gp) were provided by Dr. A. Schinkel at The Netherlands Cancer Institute (Amsterdam, The Netherlands) and used under license agreement. Cells were cultivated in Medium 199 with stable glutamine and phenol red, supplemented with 10% fetal calf serum, 100 IU/mL–100/ng/mL penicillin/streptomycin (all from Amimed, Basel, Switzerland) and 100 ng/mL colchicine at 37 °C in a humidified 5% CO_2 cell culture incubator and seeded at low density on permeable Costar1 inserts (0.33 cm^2 area, pore size 3.0 mm).

Transport measurements were performed on day 4 after seeding. The tightness of the cell monolayer was controlled with the permeability of an extracellular marker (Lucifer yellow).

The method used for *in vitro* transport studies and calculation of transport ratios was previously reported.[73] Shortly before the experiment, the culture medium was removed from the apical and basolateral compartments of the 96-insert plate and replaced with medium without phenol red. The measurement of transcellular transport was initiated by adding culture medium containing 1 μM test compound to either side (100 μL on the apical side or 240 μL on the basolateral side). The transport experiment was performed in both apical-to-basolateral and basolateral-to-apical directions in triplicates on a robotic pipetting device.

The inserts were incubated at 37 °C and 5% CO_2 and 20 μL samples were taken from both the donor and receiver sides after 3.5 h of incubation. Test compound concentrations were measured by high performance liquid chromatography–tandem mass spectrometry (LC–MS/MS). The Lucifer yellow was quantified using a Spectrafluor Plus Reader at 430/535 nm excitation/emission in each insert as a control of cell tightness. Data from inserts exhibiting marker permeation >1%/h were rejected.

***In Vivo* Measurements.** *T. b. rhodesiense* (STIB900) acute mouse model: The STIB900 acute mouse model mimics the first stage of the disease. Four female NMRI mice were used per experimental group. Each mouse was inoculated i.p. with 2.5×10^4 bloodstream forms of STIB900. Heparinized blood from a donor mouse with approximately 5×10^6 /mL parasitaemia was suspended in PSG to obtain a trypanosome suspension of 1×10^5 /mL. Each mouse was injected with 0.25 mL. The samples were formulated in 100% DMSO, first dissolved in 100% DMSO and then diluted 10 times with distilled water. Compound treatment was initiated 3 days post-infection on four consecutive days for all administration routes (i.p., p.o.) in a volume of 0.1 mL/10 g. Three mice served as infected-untreated controls. They were not injected with the vehicle alone since we have established in our labs that these vehicles do not affect parasitaemia

nor the mice. Parasitaemia was monitored using smears of tail-snip blood twice a week after treatment for two weeks followed by once a week until 60 days post-infection. Mice were considered cured when there was no parasitaemia relapse detected in the tail blood over the 60-day observation period. Mean relapse days were determined as day of relapse post-infection of mice. *In vivo* efficacy studies in mice were conducted at the Swiss Tropical and Public Health Institute (Basel) (License number 2813) according to the rules and regulations for the protection of animal rights ("Tierschutzverordnung") of the Swiss "Bundesamt für Veterinärwesen". They were approved by the veterinary office of Canton Basel-Stadt, Switzerland.

Expression and Protein-Purification of Rhodesain. Reported in Section S14 in the SI.

Incubation with Inhibitors and Crystallization of Rhodesain. Reported in Section S15 in the SI.

X-ray Diffraction Data Collection, Structure Solution and Refinement for Rhodesain. Diffraction data were collected at beamline ID29 of the ESRF Grenoble (λ = 0.97625 Å) with a Pilatus 6M detector. Data sets were processed using the XDS package[74] and Scala,[75] as summarized in Table 9. The apo-structure was solved by molecular replacement with Phaser[76] using a previously published rhodesain structure (PDB code: 2P7U[33]). The structures with inhibitor were solved using one monomer of the refined apo-structure. Alternating cycles of model building in Coot[77] and refinement using Refmac5[78] yielded the final structures. Additionally, TLS refinement was carried out in the final stages with 20 TLS groups identified by the TLSMD server[79]. Topologies for the inhibitor molecules were computed using PRODRG[80]. The quality of the obtained models was validated with Molprobity[81] and figures were prepared with PyMOL[82].

The model coordinates and structure factors for the rhodesain-inhibitor complexes have been deposited in the Protein Data Bank under the accession codes 6EX8, 6EXO and 6EXQ.

Table 9. Crystallographic Data and Refinement for the Rhodesain Crystal Structures.

	RD and 1	RD and 7	RD and 3
Data collection			
Space group	*P*1	*P*1	*P*1
Cell dimensions			
a, *b*, *c* (Å)	31.8, 49.7, 67.6	31.7, 49.8, 67.5	31.5, 50.2, 60.6
α, β, γ (°)	103.6, 98.9, 100.8	103.8, 98.9, 100.0	105.3, 96.9, 99.0
Resolution (Å)[a]	1.60 (1.69-1.60)	1.90 (2.00-1.90)	2.50 (2.64-2.50)
Completeness (%)	94.3 (93.1)	91.4 (92.0)	96.1 (96.6)
R_{meas}	0.085 (0.960)	0.091 (0.590)	0.162 (1.048)
$I / \sigma I$	10.3 (1.9)	9.2 (1.7)	6.9 (1.3)
Redundancy	3.6 (3.6)	2.2 (2.2)	3.6 (3.7)
Refinement			
Resolution (Å)	47-1.60	47-1.90	47-2.50
No. reflections	45725	26413	10975
R_{cryst} / R_{free}[b]	0.14 / 0.18	0.20 / 0.25	0.17 / 0.25
No. atoms			
Protein	3770	3658	3428
Inhibitor	72	64	68
Water	361	219	104
B factor (Å²)			
Protein	12.9	14.4	19.1
Inhibitor	36.3	50.7	75.0
Water	36.2	37.9	41.8
R.m.s deviations			

Bond lengths (Å)	0.022	0.008	0.011
Bond angles (°)	1.89	1.28	1.46
Ramachandran statistics (%)[c]	96.5/3.5/0.0	95.9/4.1/0.0	91.0/8.5/0.5

[a] Values for the highest resolution shell are shown in parentheses; [b] Five percent of the reflections were randomly omitted from refinement; [c] Ramachandran statistics indicate the fraction of residues in favored and allowed regions and outliers as defined by Molprobity[81].

Crystallization of hCatL. See Section S16 in the SI. Details on data collection, processing, and refinement statistics for derivatives **7**, **14** and **15** are listed in Table 10.

Table 10. Crystallographic Data and Refinement for the hCatL Crystal Structures.

	7 and hCatL	**14 and hCatL**	**15 and hCatL**
PDB accession number	6EZP	6F06	6EZX
Data Processing[a]			
Space Group	$P2_12_12_1$	$P2_1$	$P2_1$
Unit cell axes [Å]	54.1/60.5/70.0	43.0/50.8/84.9; β=91.5°	59.3/43.4/86.5; β=96.1°
Resolution limits [Å]	40.32-1.37 (1.41-1.37)	42.48-2.02 (2.07-2.02)	46.39-2.34 (2.40-2.34)
Completeness [%]	92.5 (86.4)	98.3 (98.9)	85.4 (84.7)
R_{merge}	0.190 (0.896)	0.127 (0.873)	0.070 (0.599)
$I/\sigma(I)$	7.2 (1.3)	5.7 (1.3)	9.5 (1.3)
Multiplicity	3.2 (3.2)	3.4 (3.4)	3.0 (3.3)
Refinement			
No. reflections	43046	22641	15249
R/R_{free} [%]	21.1/23.3	20.1/27.4	22.2/29.7
Rmsd bond length [Å]	0.012	0.015	0.010
Rmsd bond angles [°]	1.29	1.76	1.32
Ramachandran favored [%]	97.7	95.6	92.9

Ramachandran outliers [%]	0.0	0.0	0.2

[a] Number in parenthesis are values for the highest of ten resolution shells.

Chemical Synthesis. Only the synthesis and characterization of selected final compounds **1**, **19a**, **31c**, **49a** and **54b** are described herein, together with the corresponding general procedures (GP). More information about the general methods and materials, synthesis of all intermediates, and characterization, can be found in Section S17 in the SI. The purity of all compounds reported here was assessed by NMR and LC-MS, and was identified as > 95%. The NMR spectra of all reported final compounds are reported in Section S18 in the SI. The preparation of compounds **2**–**18** has been reported in [35].

General Procedures (GP). Hydrogenation (GP-1). A solution of alkene (1.0 eq) in EtOAc (17 μM) was treated with Pd/C 10% (0.1 eq) and H_2. The mixture was stirred for 4 h at 23 °C, before being filtered over celite. The filtrate was washed with brine (2x), and the organic phase was dried over Na_2SO_4, filtered, and evaporated. MPLC afforded the corresponding macrocycles.

Ring-closing Alkene Metathesis Variant 1 (GP-2). A solution of Hoveyda-Grubbs catalyst 2nd generation (0.3 eq) in dry degassed toluene was treated dropwise with a solution of diene (1.0 eq) in toluene (final concentration of 2.75 mM). The mixture was stirred for 3 h at 90 °C, before being cooled down to 23 °C. Toluene was evaporated, and the residue dissolved in EtOAc. The organic phase was washed with brine (3x), dried over Na_2SO_4, filtered, and evaporated. MPLC gave the corresponding macrocycles.

***N*-Boc Deprotection (GP-3).** A solution of protected amine (1.0 eq) in HCOOH (250 mM) was stirred for 1–4 h at 22 °C, diluted with CH_2Cl_2/H_2O 4:1, basified to pH 9, and extracted with

CH_2Cl_2 (3x). The combined organic layers were dried over Na_2SO_4, filtered, and evaporated to afford the crude corresponding amines.

Alkylation of Hydroxybenzoic Acids and 3-Iodo- or 3-Chloro-L-Tyrosine Derivatives (GP-4). A solution of carboxylic acid derivative (1.0 eq) in dry DMF, acetonitrile or acetone (290 mM) was treated with Cs_2CO_3 (2.1 eq) or K_2CO_3 (2.1 eq), stirred for 5 min at 22 °C under Ar, treated with allyl bromide (2.1 eq) or 4-bromobut-1-ene (1.1 eq), and stirred for 4–16 h. The mixture was diluted with EtOAc, washed with brine (3 x), dried over Na_2SO_4, filtered, and evaporated. The residues were purified by MPLC, or directly used in the next step.

Saponification, Variant 1 (GP-5). A solution of the ester (1.0 eq) in THF/MeOH/H_2O 2:2:1 (170 mM) was treated with LiOH (2.0 eq), stirred for 1–4 h at 22 °C, and poured onto 0.1 M HCl. The aqueous phase was extracted with CH_2Cl_2. The organic layer was dried over Na_2SO_4, filtered, and evaporated. MPLC gave the corresponding carboxylic acids, or the crude acid was directly used in the next step.

Amide Couplings (GP-6). A solution of amine (1.0 eq), carboxylic acid (1.0 eq), and HATU (2.0 eq) or TBTU (2.0 eq) in DMF (130 mM) or DMA (130 mM) was treated with *i*Pr_2NEt (4.0 eq) or Et_3N (4.0 eq), stirred for 3–18 h at 22 °C under Ar, treated with a saturated aqueous $NaHCO_3$ solution, and diluted with EtOAc. After separation of the layers, the organic phase was washed with brine (3x), dried over Na_2SO_4, filtered, and evaporated. MPLC or HPLC gave the corresponding amides.

Saponification, Variant 2 (GP-7). The crude bis-allylation product (1.0 eq) was dissolved in 5:1 EtOH/H_2O (810 mM), and treated with a 1N aqueous NaOH solution (2.0 eq). The mixture was stirred for 20 h at 80 °C, before being concentrated to remove EtOH. The resulting solution was acidified to pH 2 using 1 M aqueous HCl solution, before being extracted with CH_2Cl_2 (3x).

The combined organic layers were dried over Na_2SO_4, filtered, and evaporated. FC or MPLC gave the corresponding carboxylic acids.

Suzuki-Miyaura Cross-Coupling (GP-8). A solution of 3-iodo-L-tyrosinyl derivative (1.0 eq) in 3:1 *i*PrOH/H_2O (28 mM) was treated with potassium trifluoroborate (1.3 eq), [$PdCl_2$(dppf)CH_2Cl_2] (0.08 eq), Et_3N (2.0 eq) and Cs_2CO_3 (2.0 eq), under Ar. The mixture was stirred for 1–2 h at 90 °C, before being cooled down to 22 °C, filtered, and evaporated. MPLC afforded the corresponding macrocycles.

Ring-closing Alkene Metathesis Variant 2 (GP-9). A solution of Grubbs catalyst 2nd generation (0.3 eq) in dry degassed CH_2Cl_2 was treated dropwise with a solution of diene (1.0 eq) in CH_2Cl_2 (final concentration of ~ 1 mM). The mixture was stirred for 1–3 h at 50 °C, before being concentrated. MPLC afforded the corresponding macrocycles.

(*S*)-19-Chloro-5-oxo-8-trifluoromethyl-12,17-dioxa-4-aza-tricyclo[16.2.2.0^{6,11};]docosa-1(21),6,8,10,18(22),19-hexaene-3-carboxylic Acid (1-Cyano-cyclopropyl)-amide (1). A solution of **19a** (35 mg, 67.3 µmol) in EtOAc (4 mL) was treated with Pd/C 10% (7.16 mg, 6.73 µmol) and H_2, according to GP-1. FC (SiO_2; heptane/EtOAc, gradient from 2:1 to 1:2) gave **1** (20 mg, 57%) as a light brown solid. ^{1}H NMR (600 MHz, $CDCl_3$; 1:1 mixture of atropisomers): δ = 1.18–1.29 (m, 3 H), 1.48–1.60 (m, 3 H), 1.68–1.81 (m, 2 H), 1.87–1.93 (m, 1 H), 3.01–3.06 (m, 1 H), 3.37 (ddd, *J* = 13.9, 5.2, 2.5 Hz) and 3.45 (ddd, *J* = 14.1, 5.3, 1.9 Hz, 1 H), 3.76 (td, J = 8.8, 5.0 Hz) and 3.89 (td, J = 9.5, 4.8 Hz) (1 H), 4.96–5.06 (m, 1 H), 4.32–4.37 (m, 1 H), 4.44–4.52 (m, 1 H), 4.04 (td, *J* = 9.5, 6.3 Hz, 1 H), 6.99–7.01 (m, 0.5 H), 7.08–7.12 (m, 1.5 H), 7.19–7.21 (br. s, 2 H), 7.28–7.30 (m, 1.5 H), 7.36 (br. s, 0.5 H), 7.98 (br. s) and 7.99 ppm (br. s) (1 H). ^{13}C NMR (151 MHz, $CDCl_3$; 1:1 mixture of atropisomers): δ = 16.69 and 16.83 (1 C), 16.98 and 17.07 (1 C), 20.66 and 20.74 (1 C), 24.85 and 25.30 (1 C), 26.09 and 26.63 (1 C), 35.77 and

36.19 (1 C), 53.52 and 53.60 (1 C), 67.98 and 68.66 (1 C), 69.49 and 70.70 (1 C), 118.01–118.07 (m, 1 C), 119.70 and 119.82 (1 C), 120.05 (1 C), 121.79 (1 C), 123.39 (d, ^1J(C,F) = 273.0 Hz) and 123.39 (d, ^1J(C,F) = 273.0 Hz) (1 C), 124.99 and 125.06 (1 C), 126.68 and 126.78 (1 C), 129.53 and 129.60 (1 C), 131.02 and 131.43 (1 C), 131.85 and 131.90 (1 C), 132.24 and 132.30 (1 C), 134.79 (d, ^2J(C,F) = 14.8 Hz) and 135.00 (d, ^2J(C,F) = 14.7 Hz) (1 C), 154.31 and 154.80 (1 C), 156.72 and 156.84 (1 C), 164.86 and 165.12 (1 C), 171.75 and 172.02 ppm (1 C). HR-ESI-MS: *m/z* (%) = 522.1408 (100, $[M + H]^+$, calcd for $C_{25}H_{24}ClF_3N_3O_4^+$: 522.1402).

(*S*,*E*)-6^3-Chloro-*N*-(1-cyanocyclopropyl)-2-oxo-1^4-(trifluoromethyl)-7,12-dioxa-3-aza-1(1,2),6(1,4)-dibenzenacyclododecaphan-9-ene-4-carboxamide (19a). A solution of Hoveyda-Grubbs catalyst 2nd generation (103 mg, 164 μmol) in toluene (100 mL) was treated dropwise with **28a** (300 mg, 547 μmol) previously dissolved in toluene (100 mL), according to GP-2. FC (SiO_2; CH_2Cl_2/EtOAc, gradient from 95:5 to 60:40) gave **19a** (67 mg, 24%) as a light green foam. ^{1}H NMR (600 MHz, $CDCl_3$; 3:2 mixture of atropisomers): δ = 1.21 (ddd, *J* = 10.2, 8.0, 5.8 Hz, 0.6 H) and 1.28–1.38 (m, 1.4 H), 1.50–1.55 (m, 0.6 H) and 1.59–1.67 (m, 1.4 H), 2.92 (dd, *J* = 13.9, 6.3 Hz, 0.6 H) and 3.00 (dd, *J* = 13.9, 6.0 Hz, 0.4 H), 3.44 (dd, *J* = 13.9, 3.6 Hz, 0.4 H) and 3.58 (dd, *J* = 13.9, 2.6 Hz, 0.6 H), 4.31 (dd, *J* = 11.3, 10.4 Hz, 0.6 H), 4.43–4.54 (m, 2 H), 4.61 (qd, *J* = 11.8, 7.7 Hz, 0.8 H), 4.86 (dd, *J* = 11.4, 5.3 Hz, 0.4 H), 5.02 (ddd, *J* = 8.2, 5.9, 3.6 Hz, 0.4 H) and 5.07 (ddd, *J* = 8.6, 6.2, 2.6 Hz, 0.6 H), 5.19–5.35 (m, 1 H), 5.94 (ddd, *J* = 15.3, 9.1, 6.2 Hz, 0.4 H) and 6.10 (ddd, *J* = 15.1, 10.2, 5.0 Hz, 0.6 H), 6.82 (d, *J* = 8.1 Hz, 0.4 H), 6.85–6.94 (m, 1.4 H), 7.08 (d, *J* = 2.2 Hz, 0.6 H), 7.10–7.17 (m, 1 H), 7.21 (d, *J* = 8.3 Hz, 0.6 H), 7.27–7.38 (m, 3 H), 8.20 (d, *J* = 8.2 Hz, 0.4 H) and 8.24 ppm (d, *J* = 8.4 Hz, 0.6 H). HR-ESI-MS: *m/z* (%) = 520.1251 (100, $[M + H]^+$, calcd for $C_{25}H_{22}ClF_3N_3O_4^+$: 520.1245).

(*S*)-3-(4-(Allyloxy)-3-chlorophenyl)-2-amino-*N*-(1-cyanocyclopropyl)propanamide (20). A solution **24** (1.5 g, 3.57 mmol) in formic acid (13.7 mL, 357 mmol) was stirred at 23 °C, according to GP-3. Evaporation gave **20** (1.5 g, quant.) as a yellow oil. ^{1}H NMR (300 MHz, $CDCl_3$): δ = 1.15–1.20 (m, 2 H), 1.49–1.57 (m, 2 H), 2.79 (dd, *J* = 13.9, 8.0 Hz, 2 H), 3.05 (dd, *J* = 14.0, 4.4 Hz, 2 H), 3.57 (ddd, *J* = 8.1, 4.4, 1.2 Hz, 1 H), 4.59 (dq, *J* = 4.7, 1.5 Hz, 2 H), 5.30 (dt, *J* = 10.7, 1.5 Hz, 1 H), 5.45 (dt, *J* = 17.2, 1.5 Hz, 1 H), 6.05 (ddtd, *J* = 17.0, 10.4, 5.1, 1.2 Hz, 1 H), 6.87 (dd, *J* = 8.4, 1.2 Hz, 1 H), 7.02 (dd, *J* = 8.6, 2.1 Hz, 1 H), 7.19 (d, *J* = 2.1 Hz, 1 H), 7.80 ppm (s, 1 H). ESI-MS: *m/z* (%) = 320.0 (100, $[M + H]^+$, calcd for $C_{16}H_{19}ClN_3N_2^+$: 320.1).

Prop-2-enyl (2*S*)-3-(3-Chloro-4-prop-2-enoxyphenyl)-2-[(2-methylpropan-2-yl)oxycarbonylamino]propanoate (22). A solution of (*S*)-2-(*tert*-butoxycarbonylamino)-3-(3-chloro-4-hydroxyphenyl)propanoic acid (2.5 g, 7.92 mmol) in DMF (30 mL) was treated with Cs_2CO_3 (5.42 g, 16.6 mmol) and 3-bromoprop-1-ene (1.44 mL, 16.6 mmol), according to GP-4. FC (SiO_2; heptane/EtOAc, gradient from 100:0 to 60:40) gave **22** (1.93 g, 62%) as a light yellow oil. ^{1}H NMR (300 MHz, $CDCl_3$): δ = 1.43 (s, 9 H), 3.02 (qd, *J* = 14.1, 5.6 Hz, 2 H), 2.94–3.09 (m, 2 H), 4.51–4.63 (m, 4 H), 4.98 (d, *J* = 8.2 Hz, 1 H), 5.25–2.35 (m, 3 H), 5.45 (dd, *J* = 17.3, 1.6 Hz, 1 H), 5.81–5.95 (m, 1 H), 6.06 (ddt, *J* = 17.4, 10.3, 5.1 Hz, 1 H), 6.84 (d, *J* = 8.4 Hz, 1 H), 6.97 (dd, *J* = 8.4, 2.1 Hz, 1 H), 7.14 ppm (d, *J* = 2.1 Hz, 1 H). ESI-MS: *m/z* (%) = 296.6 (100, $[M + H - Boc]^+$, calcd for $C_{15}H_{19}ClNO_3^+$: 296.1048).

(*S*)-3-(4-(Allyloxy)-3-chlorophenyl)-2-(tert-butoxycarbonylamino)propanoic Acid (23). A solution of **22** (3.49 g, 8.82 mmol) in 2:1:1 THF/MeOH/H_2O (30 mL) was treated with LiOH (422 mg, 17.6 mmol), according to GP-5. Evaporation gave **23** (3.46 g, quant.) as a colorless oil. ^{1}H NMR (300 MHz, $CDCl_3$): δ = 1.34 (br. s, 2 H) and 1.43 (br. s, 7 H) (*t*Bu), 2.96–3.15 (m, 2 H), 4.55 (d, *J* = 7.5 Hz, 1 H), 4.59 (dt, *J* = 5.1, 1.6 Hz, 2 H), 4.93 (d, *J* = 7.8 Hz, 1 H), 5.31 (dq, *J* =

10.5, 1.5 Hz, 1 H), 5.46 (dq, J = 17.3, 1.6 Hz, 1H), 6.06 (ddt, J = 17.2, 10.3, 5.1 Hz, 1 H), 6.86 (d, J = 8.4 Hz, 1 H), 7.02 (dd, J = 8.3, 2.2 Hz, 1 H), 7.20 ppm (s, 1 H). ESI-MS: *m/z* (%) = 256.5 (100, $[M + H - Boc]^+$, calcd for $C_{12}H_{15}ClNO_3^+$: 256.0735).

***tert*-Butyl (*S*)-(3-(4-(Allyloxy)-3-chlorophenyl)-1-((1-cyanocyclopropyl)amino)-1-oxopropan-2-yl)carbamate (24).** A solution **23** (1.5 g, 4.22 mmol) in DMF (15 ml) was treated with HATU (3.21 g, 8.43 mmol), 1-aminocyclopropanecarbonitrile hydrochloride (606 mg, 5.06 mmol) and iPr$_2$NEt (2.58 mL, 14.8 mmol), according to GP-6. FC (SiO_2; heptane/EtOAc, gradient from 100:0 to 0:100) gave **24** (1.9 g, 54%) as a white solid. ^{1}H NMR (300 MHz, $CDCl_3$): δ = 1.06–1.16 (m, 2 H), 1.43 (s, 9 H), 2.97 (dd, J = 7.0, 3.5 Hz, 2 H), 4.17 (q, J = 7.3 Hz, 1 H), 4.59 (dt, J = 5.2, 1.7 Hz, 2 H), 4.96 (br. s, 1 H), 5.31 (dq, J = 10.7, 1.5 Hz, 1 H), 5.45 (dq, J = 17.2, 1.5 Hz, 1 H), 6.05 (ddt, J = 17.5, 10.4, 5.1 Hz, 1 H), 6.51 (s, 1 H), 6.87 (d, J = 8.4 Hz, 1 H), 7.03 (dd, J = 8.4, 2.3 Hz, 1 H), 7.19 ppm (d, J = 2.2 Hz, 1 H). ESI-MS: *m/z* (%) = 420.2 (100, $[M + H]^+$, calcd for $C_{21}H_{27}ClN_3O_4^+$: 420.1685).

2-Prop-2-enoxy-4-(trifluoromethyl)benzoic Acid (27a).[29] A solution of 2-hydroxy-4-(trifluoromethyl)benzoic acid (5 g, 24.3 mmol) in MeCN (30 mL) was treated with K_2CO_3 (8.38 g, 60.6 mmol) and allyl bromide (5.25 mL, 60.7 mmol), according to GP-4. Evaporation gave the bis-alkylation product **26a**, which was dissolved in 5:1 EtOH/ H_2O (30 mL), and treated with 1 M aqueous NaOH solution (1.94 g, 48.5 mmol), according to GP-7. MPLC (SiO_2; CH_2Cl_2/MeOH, gradient from 100:0 to 90:10 within 30 min) gave **27a** (4.77 g, 79%) as an off-white solid. R_f = 0.17 (SiO_2; CH_2Cl_2/MeOH 9:1). M.p. 105–108 °C. ^{1}H NMR (600 MHz, $CDCl_3$): δ = 4.85 (dt, J = 5.7, 1.3 Hz, 2 H), 5.47–5.56 (m, 2 H), 6.10 (ddt, J = 17.2, 10.5, 5.7 Hz, 1 H), 7.27 (br. s, 1 H), 7.39 (ddq, J = 8.2, 1.5, 0.6 Hz), 8.28–8.29 ppm (m, 1 H). ^{13}C NMR (150 MHz, $CDCl_3$): δ = 71.32, 110.37 (q, ^3J(C,F) = 3.8 Hz), 118.94 (q, ^3J(C,F) = 3.7 Hz), 121.36 and

121.37 (1 C), 130.45, 134.69, 136.43 (q, ^2J(C,F) = 33.0 Hz), 157.49, 164.74 ppm. $^{19}F\{^1H\}$ NMR (282 MHz, $CDCl_3$): $\delta = -63.4$ ppm. IR (ATR): $\tilde{\nu}$ = 3400–2000 (br., s), 1694 (s), 1651 (m), 1620 (m), 1582 (m), 1520 (w), 1502 (m), 1463 (s), 1453 (s), 1431 (s), 1409 (m), 1386 (m), 1378 (m), 1332 (s), 1302 (s), 1265 (m), 1234 (s), 1153 (s), 1099 (s), 1076 (s), 1026 (m), 999 (s), 935 (s), 911 (s), 859 (s), 838 (m), 785 (s), 752 (s), 700 (m), 634 (m), 620 (w), 573 (m), 542 cm^{-1} (w). HR-EI-MS: *m/z*: 246 (100, $[M]^+$, calcd for $C_{11}H_9F_3O_3^+$: 246.0498).

(*S*)-2-(Allyloxy)-*N*-(3-(4-(allyloxy)-3-chlorophenyl)-1-(1-cyanocyclopropylamino)-1-oxopropan-2-yl)-4-(trifluoromethyl)benzamide (28a). A solution of (*S*)-3-(4-(allyloxy)-3-chlorophenyl)-2-amino-*N*-(1-cyanocyclopropyl)propanamide (**20**) (180 mg, 563 µmol) in DMF (4 mL) was treated with 2-(allyloxy)-4-(trifluoromethyl)benzoic acid (**27a**; 145 mg, 591 µmol), HATU (428 mg, 1.13 mmol), and *i*Pr_2NEt (393 µL, 2.25 mmol), according to GP-6. FC (SiO_2; heptane/EtOAc, gradient from 3:1 to 2:1) gave **28a** (263 mg, 85%) as a light brown solid. ^1H NMR (600 MHz, $CDCl_3$) δ = 1.09–1.17 (m, 2 H), 1.46–1.56 (m, 2 H), 3.06–3.14 (m, 2 H), 4.58 (dt, *J* = 5.1, 1.6 Hz, 2 H), 4.71–4.74 (m, 3 H), 5.30 (dq, *J* = 10.6, 1.4 Hz, 1 H), 5.43–5.48 (m, 3 H), 6.00–6.07 (m, 2 H), 6.85 (s, 1 H), 6.87 (s, 1 H), 7.09 (dd, *J* = 8.3, 2.3 Hz, 1 H), 7.20 (s, 1 H), 7.24 (d, *J* = 2.2 Hz, 1 H), 7.35 (ddd, *J* = 8.2, 1.6, 0.7 Hz, 1 H), 8.24 (dd, *J* = 8.2, 0.9 Hz, 1 H), 8.40 ppm (d, *J* = 7.4 Hz, 1 H). ESI-MS: *m/z* (%) = 548.3 (100, $[M+H]^+$, calcd for $C_{27}H_{26}ClF_3N_3O_4^+$: 548.2).

(3*S*)-*N*-(1-Cyanocyclopropyl)-19-(1-methyl-1*H*-pyrazol-4-yl)-5-oxo-9-(trifluoromethyl)-12,17-dioxa-4-azatricyclo[16.2.2.06,11]docosa-1(20),6,8,10,18,21-hexaene-3-carboxamide (31c). A solution of **44** (23 mg, 37 µmol), potassium trifluoro(1-methyl-1*H*-pyrazol-4-yl)borate (9 mg, 49 µmol), and $[PdCl_2(dppf)CH_2Cl_2]$ (2 mg, 3 µmol) in 3:1 *i*PrOH/H_2O (1.3 mL) was treated with Et_3N (11 µL, 75 µmol) and Cs_2CO_3 (12 mg, 38 µmol), according to GP-8. MPLC

(SiO_2; CH_2Cl_2/EtOAc, gradient from 100:0 to 50:50 within 35 min) gave **31c** (10 mg, 50%) as a yellow amorphous solid. R_f = 0.10 and 0.17 (SiO_2; CH_2Cl_2/EtOAc 1:1). $[\alpha]_D^{20}$ –26.86 (*c* 0.1, $CHCl_3$). ^{1}H NMR (600 MHz, $CDCl_3$; 1:1 mixture of diastereoisomers): δ = 0.87–1.68 (m, 8 H), 2.99 (dd, *J* = 13.9, 6.6 Hz) and 3.04 (dd, *J* = 14.0, 6.4 Hz, 1 H), 3.54–3.59 (m, 1 H), 3.69 (td, *J* = 9.8, 4.6 Hz) and 3.76 (td, *J* = 9.7, 4.1 Hz, 1 H), 3.89 and 3.93 (s, 3 H), 3.98 (td, *J* = 9.9, 6.1 Hz) and 4.03–4.08 (m, 1 H), 4.22–4.26 (m) and 4.42–4.46 (m, 1 H), 4.35 (dd, *J* = 6.4, 3.9 Hz, 1 H), 4.97 (ddd, *J* = 8.2, 6.4, 4.6 Hz) and 5.03 (ddd, *J* = 8.4, 6.5, 3.5 Hz, 1 H), 6.87 (dd, *J* = 8.3, 2.3 Hz) and 7.17 (dd, *J* = 8.4, 2.2 Hz, 1 H), 6.99 (br. s) and 7.10 (br. s, 1 H), 7.07 and 7.20 (br. s, 1 H), 7.11 and 7.13 (s, 1 H), 7.23 (d, *J* = 2.6 Hz) and 7.47 (d, *J* = 2.2 Hz, 1 H), 7.29–7.32 (m, 1 H), 7.35 (d, *J* = 8.2 Hz) and 7.51 (d, *J* = 8.4 Hz, 1 H), 7.75 and 7.95 (s, 1 H), 7.76 and 8.00 (s, 1 H), 8.08 (d, *J* = 8.1 Hz) and 8.14 ppm (d, *J* = 8.0 Hz, 1 H). ^{13}C NMR (150 MHz, $CDCl_3$; 1:1 mixture of diastereoisomers): δ = 16.74, 17.07 and 17.13, 20.66 and 20.76, 24.77 and 25.32 (CH_2), 26.67 and 26.90, 35.68 and 35.78, 39.07 and 39.18, 53.64 and 53.76, 68.18 and 68.56, 68.74 and 69.87, 109.62 and 109.85, 118.06 and 118.08, 118.28 and 118.41, 119.43, 119.81 and 120.16, 121.14 and 122.52, 124.28 and 124.32, 124.53 and 124.77, 125.53 and 126.06, 128.62 and 128.80, 128.87 and 128.98, 126.54 and 129.50, 129.92 and 130.23, 132.70 and 132.85, 138.17 and 139.01, 155.60 and 155.71, 156.62 and 156.93, 164.70 and 164.99, 172.06 and 172.22 ppm. ^{19}F{^{1}H} NMR (377 MHz, $CDCl_3$; 1:1 mixture of diastereoisomers): δ = –63.12 and–63.13 ppm. IR (ATR): $\tilde{\nu}$ = 3346 (m), 3000 (m), 2945 (m), 2231 (w), 1652 (s), 1498 (s), 1423 (m), 1330 (s), 1241 (m), 1171 (m), 1125 (s), 1115 (w), 788 (m), 750 (w), 519 cm^{-1} (w). HR-ESI-MS: *m/z* (%) = 568.2189 (100, $[M + H]^+$, calcd for $C_{29}H_{29}F_3N_5O_4^+$: 568.2189).

(1^2*E*,4*S*,9*E*)-6^3-Chloro-*N*-(1-cyanocyclopropyl)-1^5-methyl-2-oxo-1^1*H*-7-oxa-3-aza-1(3,1)-pyrazola-6(1,4)-benzenacyclododecaphan-9-ene-4-carboxamide (49a). A solution of

Hoveyda-Grubbs catalyst (3.25 mg, 5.19 µmol) in toluene (40 mL) was treated with **48a** (0.05 g, 104 µmol) previously dissolved in toluene (10 mL), according to GP-2. RP-HPLC gave **49a** (15 mg, 31%) as an amorphous light brown solid. ^{1}H NMR (600 MHz, $CDCl_3$; 3:2 mixture of atropisomers): δ = 1.11–1.34 (m, 2 H), 1.43–1.62 (m, 2 H), 2.26 (d, *J* = 0.8 Hz, 1.8 H) and 2.27 (d, *J* = 0.8 Hz, 1.2 H), 2.36–2.52 (m, 2 H), 3.13 (dd, *J* = 14.4, 11.7 Hz, 0.7 H), 3.20–3.36 (m, 1.5 H), 3.99 (ddd, *J* = 14.0, 10.1, 3.7 Hz, 0.7 H), 4.05 (ddd, *J* = 14.1, 10.3, 3.7 Hz, 0.3 H), 4.12 (ddd, *J* = 14.1, 5.4, 3.9 Hz, 0.3 H), 4.19 (ddd, *J* = 14.1, 5.3, 3.6 Hz, 0.7 H), 4.28 (dt, *J* = 11.7, 5.9 Hz, 0.7 H), 4.41 (dd, *J* = 14.3, 7.2 Hz, 0.3 H), 4.51 (dt, *J* = 10.0, 6.4 Hz, 0.3 H), 4.71 (d, *J* = 4.9 Hz, 1.7 H), 4.98–5.29 (m, 1 H), 5.49–5.59 (m, 0.7 H), 5.59–5.66 (m, 0.3 H), 6.44 (d, *J* = 0.9 Hz, 0.6 H), 6.45 (s, 0.3 H), 6.53 (d, *J* = 6.1 Hz, 0.3 H), 6.61 (d, *J* = 5.7 Hz, 0.6 H), 6.80 (s) and 6.82 (2 s, 0.6 H), 6.88 and 6.90 (2 s, 0.4 H), 6.92 (d, *J* = 1.9 Hz) and 6.94 (d, *J* = 1.9 Hz, 0.3 H), 7.04 (dd, *J* = 8.3, 2.2 Hz, 0.7 H), 7.16 (dd, *J* = 2.2, 0.6 Hz, 0.7 H) and 7.27 (d, *J* = 2.2 Hz, 0.3 H), 7.94 (s, 0.3 H) and 8.12 ppm (s, 0.7 H). HR-ESI-MS: *m/z* (%) = 454.1640 (100, $[M + H]^+$, calcd for $C_{23}H_{25}ClN_5O_3^+$: 454.1640).

(4*S*,*E*)-1^6,6^3-Dichloro-*N*-(1-cyanocyclopropyl)-1^2,2-dioxo-1^1,1^2-dihydro-7-oxa-3-aza-1(3,1)-quinolina-6(1,4)-benzenacycloundecaphan-9-ene-4-carboxamide (54b). A solution of Hoveyda-Grubbs catalyst second generation (30.3 mg, 48.4 µmol) in toluene (65 mL) was treated with **53b** (0.08 g, 161 µmol) previously dissolved in toluene (15 mL), according to GP-2. FC (SiO_2; heptane/EtOAc, gradient from 60:40 to 70:30) gave **54b** (15 mg, 26%) as an amorphous light gray solid. ^{1}H NMR (600 MHz, $(CD_3)_2SO$; 1:1 mixture of atropisomers): δ = 1.19–1.33 (m, 2 H), 1.49–1.62 (m, 2 H), 2.87 (dd, *J* = 13.8, 8.9 Hz, 0.5 H), 2.99 (d, *J* = 4.9 Hz, 1 H), 3.20 (dd, *J* = 13.8, 6.6 Hz, 0.5 H), 4.30–4.58 (m, 0.5 H), 4.65–4.77 (m, 0.5 H), 4.82 (ddt, *J* = 20.8, 8.4, 4.7 Hz, 4 H), 4.92–5.03 (m, 0.5 H), 5.38–5.52 (m, 0.5 H), 5.54–5.68 (m, 0.5 H), 5.81

(dt, J = 15.6, 5.3 Hz, 0.5 H), 6.35 (dd, J = 8.4, 2.2 Hz, 0.5 H), 6.66 (d, J = 8.5 Hz, 0.5 H), 6.73 (dd, J = 8.3, 2.2 Hz, 0.5 H), 6.86 (d, J = 8.4 Hz, 0.5. H), 6.92 (d, J = 2.2 Hz, 0.5 H), 7.01 (d, J = 2.1 Hz, 0.5 H), 7.73–7.83 (m, 1.5 H), 7.91 (s) and 7.92 (s, 0.5 H), 8.20 (d, J = 2.5 Hz, 0.5 H) and 8.21 (d, J = 2.5 Hz, 0.5 H), 8.80 (s, 0.5 H) and 8.86 (s, 0.5 H), 8.96 (s, 0.5 H) and 9.23 (s, 0.5 H), 9.46 (d, J = 7.5 Hz, 0.5 H) and 9.50 ppm (d, J = 8.9 Hz, 0.5 H). HR-ESI-MS: *m/z* (%) = 537.1092 (100, $[M + H]^+$, calcd for $C_{27}H_{23}Cl_2N_4O_4^+$: 537.1091).

ASSOCIATED CONTENT

Supporting Information. Results from the initial screening; Polar surface area calculations; Additional figures and schemes on predicted protein-ligand interactions by modeling; Atropisomerism; X-ray Crystal Structures of RD and hCatL; Exposure in blood; Metabolic stability studies; Linker modification; Antiparasitic activity against a parasite panel; Brain penetration; Reversibility of drug effects; Synthetic procedures and characterization; NMR spectra of all final compounds, Molecular formula strings. This material is available free of charge via the Internet at http://pubs.acs.org.

AUTHOR INFORMATION

Corresponding Author

*FD: Phone +41 44 63 22992. E-mail: diederich@org.chem.ethz.ch

*WH: Phone +41 61 68 88693. E-mail: wolfgang.haap@roche.com.

Author Contributions

The manuscript was written through contributions of all authors. All authors have given approval to the final version of the manuscript. #M.G. and U.D. contributed equally.

Funding Sources

Work was supported by F. Hoffmann-La Roche Ltd. and by an F. Hoffmann-La Roche – ETH Zurich research agreement, by ETH Zürich, and by the Collaborative Research Center 630 (German Research Society, DFG).

ACKNOWLEDGMENT

The authors acknowledge Markus Buerkler and Dr. Inken Plitzko from the Roche Analytics Service for measuring all NMR data, and Daniel Zimmerli for measuring the optical rotation. Björn Wagner and Virginie Micallef are acknowledged for physicochemical characterization of the compounds. We thank Martine Stihle for support for the hCatL crystallization experiments. *In vitro* transport studies were performed by Marie-Elise Brun and Dr. Silke Simon, and pharmacokinetic studies were conducted by Thomas Thelly, Marie-Stella Gruyer, Christelle Rapp, Véronique Dall'Asen and Christophe Flament. We thank Nicole Denk, Sabine Maehrlein, and Ulrike Nowe at the Johannes-Gutenberg Universität Mainz for support with the enzymatic assays, Christiane Braghiroli, Monica Cal and Sonja Keller for help with the parasitic assays, and the staff of beamline ID29 at the European Synchrotron Radiation Facility (ESRF) for technical support.

ABBREVIATIONS

Boc, *tert*-Butoxycarbonyl; CDI, 1,1'-carbonyldiimidazole; dba, (1*E*, 4*E*)-1,5-diphenylpenta-1,4-dien-3-one; DBU, 2,3,4,6,7,8,9,10-octahydropyrimido[1,2-a]azepine; DCHA, dicyclohexylamine; DMA, *N,N*-dimethylacetamide; DMF, *N,N*-dimethylformamide; dppf, 1,1'-bis(diphenylphosphanyl) ferrocene; DMSO, dimethylsulfoxide; HATU, 1-[bis(dimethylamino)methylene]-1*H*-1,2,3-triazolo[4,5-b]pyridinium 3-oxide hexafluorophosphate; HPLC, high pressure liquid chromatography; FC, flash chromatography; *m*CPBA, 3-chloroperbenzoic acid; Ra-Ni, Raney nickel; RuPhos = 2-Dicyclohexylphosphino-2′,6′-diisopropoxybiphenyl; TBTU = *O*-(Benzotriazol-1-yl)-*N,N,N′,N′*-tetramethyluronium tetrafluoroborate; THF, tetrahydrofuran.

Authors will release the atomic coordinates and experimental data upon article publication.

PDB ID	Compound Number
6EX8	**1**
6EXO	**7**
6EXQ	**3**
6EZP	**7**
6EZX	**15**
6F06	**14**

REFERENCES

(1) Brun, R.; Blum, J.; Chappuis, F.; Burri, C. Human African Trypanosomiasis. *Lancet* **2010**, *375*, 148-159.

(2) Feasey, N.; Wansbrough-Jones, M.; Mabey, D. C. W.; Solomon, A. W. Neglected Tropical Diseases. *Br. Med. Bull.* **2010**, *93*, 179-200.

(3) Malvy, D.; Chappuis, F. Sleeping Sickness. *Clin. Microbiol. Infect.* **2011**, *17*, 986-995.

(4) Priotto, G.; Kasparian, S.; Mutombo, W.; Ngouama, D.; Ghorashian, S.; Arnold, U.; Ghabri, S.; Baudin, E.; Buard, V.; Kazadi-Kyanza, S.; Ilunga, M.; Mutangala, W.; Pohlig, G.; Schmid, C.; Karunakara, U.; Torreele, E.; Kande, V. Nifurtimox-Eflornithine Combination Therapy for Second-stage African *Trypanosoma brucei gambiense* Trypanosomiasis: A Multicentre, Randomised, Phase III, Non-inferiority Trial. *Lancet* **2009**, *374*, 56-64.

(5) Volkov, O. A.; Brockway, A. J.; Wring, S. A.; Peel, M.; Chen, Z.; Phillips, M. A.; De Brabander, J. K. Species-Selective Pyrimidineamine Inhibitors of *Trypanosoma brucei* S-Adenosylmethionine Decarboxylase. *J. Med. Chem.* **2018**, *61*, 1182-1203.

(6) Fueyo González, F. G.; Ebiloma, G. U.; Izquierdo García, C.; Bruggeman, V.; Sánchez Villamañán, J. M.; Donachie, A.; Oluwadare Balogun, E.; Inaoka, D. K.; Shiba, T.; Harada, S.; Kita, K.; de Koning, H. P.; Dardonville, C. Conjugates of 2,4-Dihydroxybenzoate and Salicylhydroxamate and Lipocations Display Potent Antiparasite Effects by Efficiently Targeting the *Trypanosoma brucei* and *Trypanosoma congolense* Mitochondrion. *J. Med. Chem.* **2017**, *60*, 1509-1522.

(7) Patrick, D. A.; Gillespie, J. R.; McQueen, J.; Hulverson, M. A.; Ranade, R. M.; Creason, S. A.; Herbst, Z. M.; Gelb, M. H.; Buckner, F. S.; Tidwell, R. R. Urea Derivatives of 2-Aryl-benzothiazol-5-amines: A New Class of Potential Drugs for Human African Trypanosomiasis. *J. Med. Chem.* **2017**, *60*, 957-971.

(8) Russell, S.; Rahmani, R.; Jones, A. J.; Newson, H. L.; Neilde, K.; Cotillo, I.; Rahmani Khajouei, M.; Ferrins, L.; Qureishi, S.; Nguyen, N.; Martinez-Martinez, M. S.; Weaver, D. F.; Kaiser, M.; Riley, J.; Thomas, J.; De Rycker, M.; Read, K. D.; Flematti, G. R.; Ryan, E.; Tanghe, S.; Rodriguez, A.; Charman, S. A.; Kessler, A.; Avery, V. M.; Baell, J. B.; Piggott, M. J. Hit-to-Lead Optimization of a Novel Class of Potent, Broad-Spectrum Trypanosomacides. *J. Med. Chem.* **2016**, *59*, 9686-9720.

(9) Cleghorn, L. A. T.; Albrecht, S.; Stojanovski, L.; Simeons, F. R. J.; Norval, S.; Kime, R.; Collie, I. T.; De Rycker, M.; Campbell, L.; Hallyburton, I.; Frearson, J. A.; Wyatt, P. G.; Read, K. D.; Gilbert, I. H. Discovery of Indoline-2-carboxamide Derivatives as a New Class of Brain-Penetrant Inhibitors of *Trypanosoma brucei*. *J. Med. Chem.* **2015**, *58*, 7695-7706.

(10) Jorgensen, W. L. Challenges for Academic Drug Discovery. *Angew. Chem., Int. Ed.* **2012**, *51*, 11680-11684.

(11) Fonteilles-Drabek, S.; Reddy, D.; Wells, T. N. C. Managing Intellectual Property to Develop Medicines for the World's Poorest. *Nat. Rev. Drug Discov.* **2017**, *16*, 223-224.

(12) Klug, D. M.; Gelb, M. H.; Pollastri, M. P. Repurposing Strategies for Tropical Disease Drug Discovery. *Bioorg. Med. Chem. Lett.* **2016**, *26*, 2569-2576.

(13) Kaiser, M.; Bray, M. A.; Cal, M.; Bourdin Trunz, B.; Torreele, E.; Brun, R. Antitrypanosomal Activity of Fexinidazole, a New Oral Nitroimidazole Drug Candidate for Treatment of Sleeping Sickness. *Antimicrob. Agents Chemother.* **2011**, *55*, 5602-5608.

(14) Torreele, E.; Bourdin Trunz, B.; Tweats, D.; Kaiser, M.; Brun, R.; Mazué, G.; Bray, M. A.; Pécoul, B. Fexinidazole – A New Oral Nitroimidazole Drug Candidate Entering Clinical Development for the Treatment of Sleeping Sickness. *PLoS Negl. Trop. Dis.* **2010**, *4 (12)*, e923.

(15) Ding, D.; Zhao, Y.; Meng, Q.; Xie, D.; Nare, B.; Chen, D.; Bacchi, C. J.; Yarlett, N.; Zhang, Y.-K.; Hernandez, V.; Xia, Y.; Freund, Y.; Abdulla, M.; Ang, K.-H.; Ratnam, J.; McKerrow, J. H.; Jacobs, R. T.; Zhou, H.; Plattner, J. J. Discovery of Novel Benzoxaborole-Based Potent Antitrypanosomal Agents. *ACS Med. Chem. Lett.* **2010**, *1*, 165-169.

(16) Jones, D. C.; Foth, B. J.; Urbaniak, M. D.; Patterson, S.; Ong, H. B.; Berriman, M.; Fairlamb, A. H. Genomic and Proteomic Studies on The Mode of Action of Oxaboroles Against The African Trypanosome. *PLoS Negl. Trop. Dis.* **2015**, *9 (12)*, e0004299.

(17) DND*i* Clinical Trials Home Page. https://www.dndi.org/2016/clinical-trials/clinical-trials-hat/ (accessed April 2, 2017).

(18) Nicoll-Griffith, D. A. Use of Cysteine-reactive Small Molecules in Drug Discovery for Trypanosomal Disease. *Expert Opin. Drug Disc.* **2012**, *7*, 353-366.

(19) Ferreira, L. G.; Andricopulo, A. D. Targeting Cysteine Proteases in Trypanosomatid Disease Drug Discovery. *Pharmacol. Ther.* **2018**, *180*, 49-61.

(20) Redecke, L.; Nass, K.; DePonte, D. P.; White, T. A.; Rehders, D.; Barty, A.; Stellato, F.; Liang, M.; Barends, T. R. M.; Boutet, S.; Williams, G. J.; Messerschmidt, M.; Seibert, M. M.; Aquila, A.; Arnlund, D.; Bajt, S.; Barth, T.; Bogan, M. J.; Caleman, C.; Chao, T.-C.; Doak, R. B.; Fleckenstein, H.; Frank, M.; Fromme, R.; Galli, L.; Grotjohann, I.; Hunter, M. S.; Johansson, L. C.; Kassemeyer, S.; Katona, G.; Kirian, R. A.; Koopmann, R.; Kupitz, C.; Lomb, L.; Martin, A. V.; Mogk, S.; Neutze, R.; Shoeman, R. L.; Steinbrener, J.; Timneanu, N.; Wang, D.; Weierstall, U.; Zatsepin, N. A.; Spence, J. C. H.; Fromme, P.; Schlichting, I.; Duszenko, M.; Betzel, C.; Chapman, H. N. Natively Inhibited *Trypanosoma brucei* Cathepsin B Structure Determined by Using an X-ray Laser. *Science* **2013**, *339*, 227–230.

(21) Mackey, Z. B.; O'Brien, T. C.; Greenbaum, D. C.; Blank, R. B.; McKerrow, J. H. A Cathepsin B-like Protease Is Required for Host Protein Degradation in *Trypanosoma brucei*. *J. Biol. Chem.* **2004**, *279*, 48426-48433.

(22) Kerr, I. D.; Wu, P.; Marion-Tsukamaki, R.; Mackey, Z. B.; Brinen, L. S. Crystal Structures of TbCatB and Rhodesain, Potential Chemotherapeutic Targets and Major Cysteine Proteases of *Trypanosoma brucei*. *PLoS Negl. Trop. Dis.* **2010**, *4(6)*, e701.

(23) Reyes-López, M.; Piña-Vázquez C.; Serrano-Luna J. Transferrin: Endocytosis and Cell Signaling in Parasitic Protozoa. *BioMed Research International*, **2015**, Article ID 641392.

(24) Caffrey, C. R.; Hansell, E.; Lucas, K. D.; Brinen, L. S.; Alvarez Hernandez, A.; Cheng, J.; Gwaltney, S. L. II; Roush, W. R.; Stierhof, Y.-D.; Bogyo, M.; Steverding, D.; McKerrow, J. H. Active Site Mapping, Biochemical Properties and Subcellular Localization of Rhodesain, the Major Cysteine Protease of *Trypanosoma brucei rhodesiense*. *Mol. Biochem. Parasitol.* **2001**, *118*, 61-73.

(25) Overath, P.; Chaudhri, M.; Steverding, D.; Ziegelbauer, K. Invariant Surface Proteins in Bloodstream Forms of *Trypanosoma brucei*. *Parasitol. Today* **1994**, *10*, 53-58.

(26) Lonsdale-Eccles, J. D.; Grab, D. J. Trypanosome Hydrolases and the Blood-brain Barrier. *Trends Parasitol.* **2002**, *18*, 17-19.

(27) Siklos, M.; BenAissa, M.; Thatcher, G. R. J. Cysteine Proteases as Therapeutic Targets: Does Selectivity Matter? A Systematic Review of Calpain and Cathepsin Inhibitors. *Acta Pharmaceutica Sinica B* **2015**, *5*, 506-519.

(28) Lv, B.-J.; Lindholt, J. S.; Wang, J.; Cheng, X.; Shi, G.-P. Plasma Levels of Cathepsins L, K, and V and Risks of Abdominal Aortic Aneurysms: A Randomized Population-based Study. *Atherosclerosis* **2013**, *230*, 100-105.

(29) Zhang, L.; Wei, L.; Shen, G.; He, B.; Gong, W.; Min, N.; Zhang, L.; Duan, Y.; Xie, J.; Luo, H.; Gao, X. Cathepsin L Is Involved in Proliferation and Invasion of Ovarian Cancer Cells. *Mol. Med. Rep.* **2015**, *11*, 468-474.

(30) Sudhan, D. R.; Rabaglino, M. B.; Wood, C. E.; Siemann, D. W. Cathepsin L in Tumor Angiogenesis and its Therapeutic Intervention by the Small Molecule Inhibitor KGP94. *Clin. Exp. Metastasis*, **2016**, *33*, 461-473.

(31) Olson, O. C.; Joyce, J. A. Cysteine Cathepsin Proteases: Regulators of Cancer Progression and Therapeutic Response. *Nat. Rev. Cancer.* **2015**, *15*, 712-729.

(32) Wang, H.; Sang, N.; Zhang, C.; Raghupathi, R.; Tanzi, R. E.; Saunders, A. Cathepsin L Mediates the Degradation of Novel APP C-Terminal Fragments. *Biochemistry* **2015**, *54*, 2806-2816.

(33) Kerr, I. D.; Lee, J. H.; Farady, C. J.; Marion, R.; Rickert, M.; Sajid, M.; Pandey, K. C.; Caffrey, C. R.; Legac, J.; Hansell, E.; McKerrow, J. H.; Craik, C. S.; Rosenthal, P. J.; Brinen, L. S. Vinyl Sulfones as Antiparasitic Agents and a Structural Basis for Drug Design. *J. Biol. Chem.* **2009**, *284*, 25697-25703.

(34) Di, L.; Rong, H.; Feng, B. Demystifying Brain Penetration in Central Nervous System Drug Discovery. *J. Med. Chem.* **2013**, *56*, 2-12.

(35) Anselm, L.; Banner, D.; Blanc, J.-B.; Gaufreteau, D.; Haap, W.; Hartmann, G.; Kuhn, B.; Luebbers, T.; Peters, J.-U.; Spinnler, B. Macrocyclic Amides as Protease Inhibitors. PCT/EP2013/050204, 2013.

(36) Ehmke, V.; Heindl, C.; Rottmann, M.; Freymond, C.; Schweizer, W. B.; Brun, R.; Stich, A.; Schirmeister, T.; Diederich, F. Potent and Selective Inhibition of Cysteine Proteases from *Plasmodium falciparum* and *Trypanosoma brucei*. *ChemMedChem* **2011**, *6*, 273-278.

(37) Giroud, M.; Harder, M.; Kuhn, B.; Haap, W.; Trapp, N.; Schweizer, W. B.; Schirmeister, T.; Diederich, F. Fluorine Scan of Inhibitors of the Cysteine Protease Human Cathepsin

L: Dipolar and Quadrupolar Effects in the π-Stacking of Fluorinated Phenyl Rings on Peptide Amide Bonds. *ChemMedChem* **2016**, *11*, 1042-1047.

(38) Giroud, M.; Ivkovic, J.; Martignoni, M.; Fleuti, M.; Trapp, N.; Haap, W.; Kuglstatter, A.; Benz, J.; Kuhn, B.; Schirmeister, T.; Diederich, F. Inhibition of the Cysteine Protease Human Cathepsin L by Triazine Nitriles: Amide□□□Heteroarene π-Stacking Interactions and Chalcogen Bonding in the S3 Pocket. *ChemMedChem* **2017**, *12*, 257-270.

(39) Hardegger, L. A.; Kuhn, B.; Spinnler, B.; Anselm, L.; Ecabert, R.; Stihle, M.; Gsell, B.; Thoma, R.; Diez, J.; Benz, J.; Plancher, J.-M.; Hartmann, G.; Banner, D. W.; Haap, W.; Diederich, F. Systematic Investigation of Halogen Bonding in Protein–Ligand Interactions. *Angew. Chem., Int. Ed.* **2011,** *50*, 314-318.

(40) Räz, B.; Iten, M.; Grether-Bühler, Y.; Kaminsky, R.; Brun, R. The Alamar Blue® Assay to Determine Drug Sensitivity of African Trypanosomes (*T.b. rhodesiense* and *T.b. gambiense*) In Vitro. *Acta Tropica* **1997**, *68*, 139-147.

(41) Nwaka, S.; Ramirez, B.; Brun, R.; Maes, L.; Douglas, F.; Ridley, R. Advancing Drug Innovation for Neglected Diseases – Criteria for Lead Progression. *PLoS Negl. Trop. Dis.* **2009**, *3* (8), e440.

(42) Wager, T. T.; Hou, X.; Verhoest, P. R.; Villalobos, A. Moving Beyond Rules: The Development of a Central Nervous System Multiparameter Optimization (CNS MPO) Approach To Enable Alignment of Druglike Properties. *ACS Chem. Neurosci.* **2010**, *1*, 435-449.

(43) Kuhn, B.; Mohr, P.; Stahl, M. Intramolecular Hydrogen Bonding in Medicinal Chemistry. *J. Med. Chem.* **2010**, *53*, 2601-2611.

(44) Giordanetto, F.; Tyrchan, C.; Ulander, J. Intramolecular Hydrogen Bond Expectations in Medicinal Chemistry. *ACS Med. Chem. Lett.* **2017**, *8*, 139-142.

(45) Dufour, E.; Storer, A. C.; Ménard, R. Peptide Aldehydes and Nitriles as Transition State Analog Inhibitors of Cysteine Proteases. *Biochemistry* **1995**, *34*, 9136-9143.

(46) Gerber, P. R.; Müller, K. MAB, A Generally Applicable Molecular Force Field for Structure Modelling in Medicinal Chemistry. *J. Comput.-Aided Mol. Des.* **1995**, *9*, 251-268.

(47) Hong, S. H.; Day, M. W.; Grubbs, R. H. Decomposition of a Key Intermediate in Ruthenium-Catalyzed Olefin Metathesis Reactions. *J. Am. Chem. Soc.* **2004**, *126*, 7414-7415.

(48) Garber, S. B.; Kingsbury, J. S.; Gray, B. L.; Hoveyda, A. H. Efficient and Recyclable Monomeric and Dendritic Ru-Based Metathesis Catalysts. *J. Am. Chem. Soc.* **2000**, *122*, 8168-8179.

(49) Cochrane, J. R.; White, J. M.; Wille, U.; Hutton, C. A. Total Synthesis of Mycocyclosin. *Org. Lett.* **2012,** *14*, 2402-2405.

(50) Molander, G. A.; Canturk, B.; Kennedy, L. Scope of the Suzuki-Miyaura Cross-Coupling Reactions of Potassium Heteroaryltrifluoroborates. *J. Org. Chem.* **2009**, *74*, 973-980.

(51) Brameld, K. A.; Kuhn, B.; Reuter, D. C.; Stahl, M. Small Molecule Conformational Preferences Derived from Crystal Structure Data. A Medicinal Chemistry Focused Analysis. *J. Chem. Inf. Model.* **2008**, *48*, 1-24.

(52) Eliel, E. L.; Wilen, S. H.; Mander, L. N. *Stereochemistry of Organic Compounds;* John Wiley & Sons, Inc.: New York, 1994; Chapt. 14, pp. 1119-1190.

(53) Ōki, M. Recent Advances in Atropisomerism. In *Topics in Stereochemistry*; Allinger, N. L.; Eliel E. L.; Wilen, S. H., Eds.; Wiley: New York, 1983; Vol 14, pp 1-81.

(54) LaPlante, S. R.; D. Fader, L.; Fandrick, K. R.; Fandrick, D. R.; Hucke, O.; Kemper, R.; Miller, S. P. F.; Edwards, P. J. Assessing Atropisomer Axial Chirality in Drug Discovery and Development. *J. Med. Chem.* **2011**, *54*, 7005-7022.

(55) Glunz, P. W.; Mueller, L.; Cheney, D. L.; Ladziata, V.; Zou, Y.; Wurtz, N. R.; Wei, A.; Wong, P. C.; Wexler, R. R.; Priestley, E. S. Atropisomer Control in Macrocyclic Factor VIIa Inhibitors. *J. Med. Chem.* **2016**, *59*, 4007-4018.

(56) LaPlante, S. R.; Forgione, P.; Boucher, C.; Coulombe, R.; Gillard, J.; Hucke, O.; Jakalian, A.; Joly, M.-A.; Kukolj, G.; Lemke, C.; McCollum, R.; Titolo, S.; Beaulieu, P. L.; Stammers, T. Enantiomeric Atropisomers Inhibit HCV Polymerase and/or HIV Matrix: Characterizing Hindered Bond Rotations and Target Selectivity. *J. Med. Chem.* **2014**, *57*, 1944-1951.

(57) Ehmke, V.; Winkler, E.; Banner, D. W.; Haap, W.; Schweizer, W. B.; Rottmann, M.; Kaiser, M.; Freymond, C.; Schirmeister, T.; Diederich, F. Optimization of Triazine Nitriles as Rhodesain Inhibitors: Structure–Activity Relationships, Bioisosteric

Imidazopyridine Nitriles, and X-ray Crystal Structure Analysis with Human Cathepsin L. *ChemMedChem* **2013**, *8*, 967-975.

(58) Asaad, N.; Bethel, P. A.; Coulson, M. D.; Dawson, J. E.; Ford, S. J.; Gerhardt, S.; Grist, M.; Hamlin, G. A.; James, M. J.; Jones, E. V.; Karoutchi, G. I.; Kenny, P. W.; Morley, A. D.; Oldham, K.; Rankine, N.; Ryan, D.; Wells, S. L.; Wood, L.; Augustin, M.; Krapp, S.; Simader, H.; Steinbacher, S. Dipeptidyl Nitrile Inhibitors of Cathepsin L. *Bioorg. Med. Chem. Lett.* **2009**, *19*, 4280-4283.

(59) Claiborne, A.; Yeh, J. I.; Mallett, T. C.; Luba, J.; Crane, E. J. III; Charrier, V.; Parsonage, D. Protein-Sulfenic Acids: Diverse Roles for an Unlikely Player in Enzyme Catalysis and Redox Regulation. *Biochemistry* **1999**, *38*, 15407-15416.

(60) Kulathu, Y.; Garcia, F. J.; Mevissen, T. E. T.; Busch, M.; Arnaudo, N.; Carroll, K. S.; Barford, D.; Komander, D. Regulation of A20 and Other OUT Deubiquitinases by Reversible Oxidation. *Nat. Commun.* **2013**, *4*, 1569.

(61) Fürstner, A. Alkyne Metathesis on the Rise. *Angew. Chem., Int. Ed.* **2013**, *52*, 2794-2819.

(62) Avelar, L. A. A.; Camilo, C. D.; de Albuquerque, S.; Fernandes, W. B.; Gonçalez, C.; Kenny, P. W.; Leitão, A.; McKerrow, J. H.; Montanari, C. A.; Meñaca Orozco, E. V.; Ribeiro, J. F. R.; Rocha, J. R.; Rosini, F.; Saidel, M. E. Molecular Design, Synthesis and Trypanocidal Activity of Dipeptidyl Nitriles as Cruzain Inhibitors. *PLoS Negl. Trop. Dis.* **2015**, *9* (7), e0003916.

(63) Almeida, M. S.; Santini Pereira, B. A.; Lopes Ribeiro-Guimarães, M; Alves, C. R. Proteinases as Virulence Factors in *Leishmania* spp. Infection in Mammals. *Parasit. Vectors* **2012**, *5*, 160.

(64) Caruso, A.; Alvarez-Sánchez, R.; Hillebrecht, A.; Poirier, A.; Schuler, F.; Lavé, T.; Funk, C.; Belli, S. PK/PD Assessment in CNS Drug Discovery: Prediction of CSF Concentration in Rodents for P-glycoprotein Substrates and Application to In Vivo Potency Estimation. *Biochem. Pharmacol.* **2013**, *85*, 1684-1699.

(65) Isabel, E.; Mellon, C.; Boyd, M. J.; Chauret, N.; Deschênes, D.; Desmarais, S.; Falgueyret, J.-P.; Gauthier, J. Y.; Khougaz, K.; Lau, C. K.; Léger, S.; Levorse, D. A.; Li, C. S.; Massé, F.; David Percival, M.; Roy, B.; Scheigetz, J.; Thérien, M.; Truong, V. L.; Wesolowski, G.; Young, R. N.; Zamboni, R.; Cameron Black, W. Difluoroethylamines as an Amide Isostere in Inhibitors of Cathepsin K. *Bioorg. Med. Chem. Lett.* **2011**, *21*, 920-923.

(66) Orhan, I.; Şener, B.; Kaiser, M.; Brun, R.; Tasdemir, D. Inhibitory Activity of Marine Sponge-Derived Natural Products against Parasitic Protozoa. *Mar. Drugs* **2010**, *8*(1), 47-58.

(67) Cheng, Y.-C.; Prusoff, W. H. Relationship Between The Inhibition Constant (K_i) and the Concentration of Inhibitor Which Causes 50 Per Cent Inhibition (IC_{50}) of an Enzymatic Reaction. *Biochem. Pharmacol.* **1973**, *22*, 3099-3108.

(68) Schirmeister, T.; Schmitz, J.; Jung, S.; Schmenger, T.; Krauth-Siegel, R. L.; Gütschow, M. Evaluation of Dipeptide Nitriles as Inhibitors of Rhodesain, A Major Cysteine Protease of *Trypanosoma brucei*. *Bioorg. Med. Chem. Lett.* **2017**, *27*, 45-50.

(69) Wagner, B.; Fischer, H.; Kansy, M.; Seelig, A.; Assmus, F. Carrier Mediated Distribution System (CAMDIS): A New Approach for the Measurement of Octanol/Water Distribution Coefficients. *Eur. J. Pharm. Sci.* **2015**, *68*, 68-77.

(70) Kansy, M.; Senner, F.; Gubernator, K. Physicochemical High Throughput Screening: Parallel Artificial Membrane Permeation Assay in the Description of Passive Absorption Processes. *J. Med. Chem.* **1998**, *41*, 1007-1010.

(71) Wuitschik, G.; Carreira, E. M.; Wagner, B.; Fischer, H.; Parrilla, I.; Schuler, F.; Rogers-Evans, M.; Müller, K. Oxetanes in Drug Discovery: Structural and Synthetic Insights. *J. Med. Chem.* **2010**, *53*, 3227-3246.

(72) Fowler, S.; Zhang, H. *In Vitro* Evaluation of Reversible and Irreversible Cytochrome P450 Inhibition: Current Status on Methodologies and their Utility for Predicting Drug–Drug Interactions. *AAPS J.* **2008**, *10*, 410-424.

(73) Schwab, D.; Fischer, H.; Tabatabaei, A.; Poli, S.; Huwyler, J. Comparison of in Vitro P-Glycoprotein Screening Assays: Recommendations for Their Use in Drug Discovery. *J. Med. Chem.* **2003**, *46*, 1716-1725.

(74) Kabsch, W. *XDS. Acta Cryst.* D. **2010***, 66,* 125-132.

(75) Evans, P.R. Scaling and Assessment of Data Quality. *Acta Cryst.* **2006**, *D62*, 72-82.

(76) McCoy, A. J.; Grosse-Kunstleve, R. W.; Adams, P. D.; Winn, M. D.; Storoni, L. C.; Read, R. J. *Phaser* Crystallographic Software. *J. Appl. Crystallogr.* **2007**, *40*, 658-674.

(77) Emsley, P.; Lohkamp, B.; Scott, W. G.; Cowtan, K. Features and Development of Coot. *Acta Cryst.* **2010**, *D66*, 486-501.

(78) Murshudov, G. N.; Skubák P.; Lebedev, A. A.; Pannu, N. S.; Steiner, R. A.; Nicholls, R. A.; Winn, M. D.; Long, F.; Vagin, A. A. REFMAC5 for the Refinement of Macromolecular Crystal Structures. *Acta Cryst.* **2011**, *D67*, 355-367.

(79) Painter, J.; Merritt, E. A. TLSMD Web Server for the Generation of Multi-group TLS Models. *J. Appl. Cryst.* **2006**, *39*, 109-111.

(80) Schüttelkopf, A. W.; van Aalten, D. M. F. PRODRG: A Tool for High-throughput Crystallography of Protein-ligand Complexes. *Acta Crystallogr.* **2004**, *D60*, 1355-1363.

(81) Chen, V. B.; Arendall, W. B. 3rd; Headd, J. J.; Keedy, D. A.; Immormino, R. M.; Kapral, G. J.; Murray, L. W.; Richardson, J. S.; Richardson, D. C. MolProbity: All-atom Structure Validation for Macromolecular Crystallography. *Acta Cryst* **2010**, *D66*, 12-21.

(82) DeLano, W. L. (2002): The PyMOL Molecular Graphics System. From http://www.pymol.org.

TABLE OF CONTENTS GRAPHIC

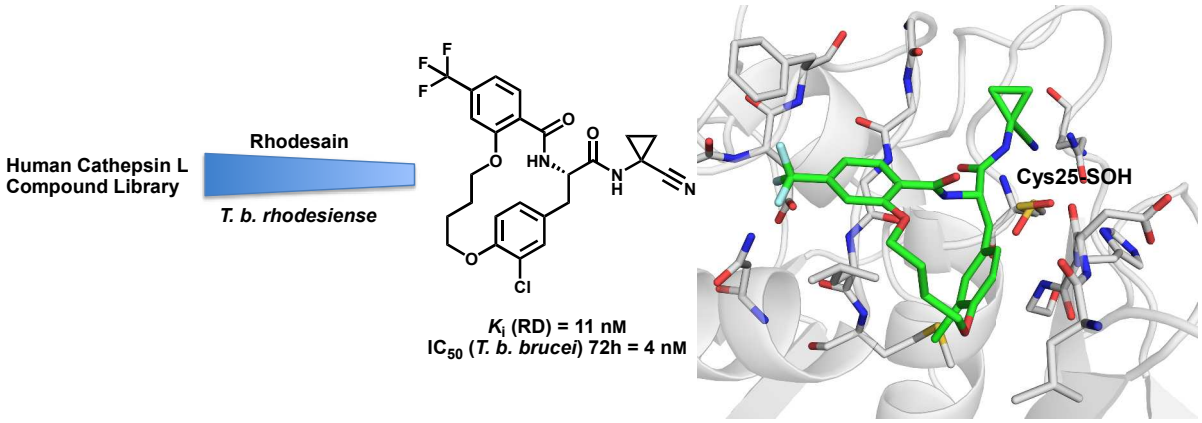

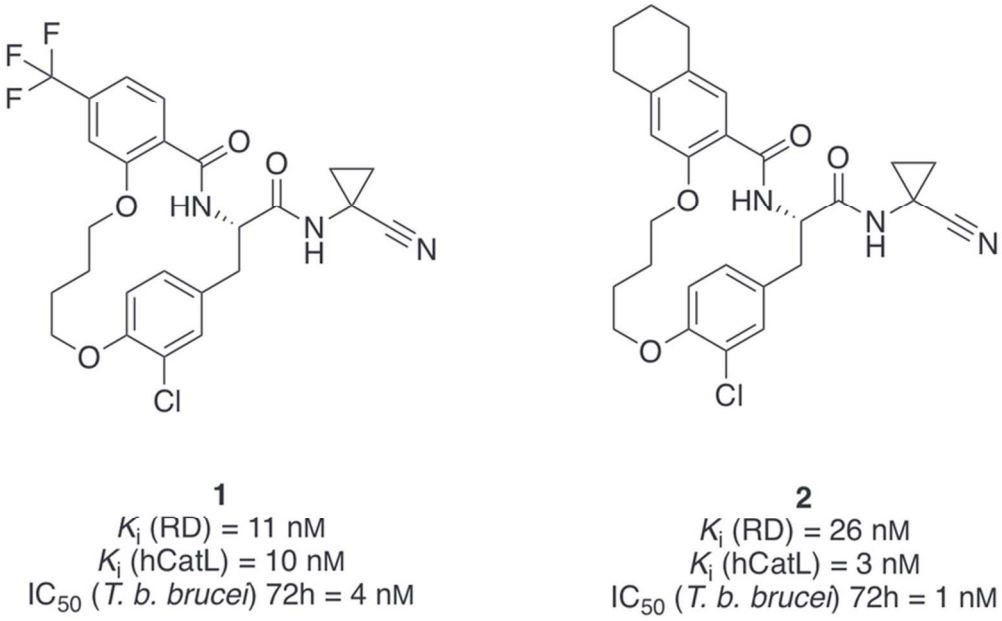

Figure 1. Structure of the two hits 1 and 2 and their binding affinities for RD and hCatL, respectively, as well as the cell-growth inhibition of T. b. brucei.

72x45mm (300 x 300 DPI)

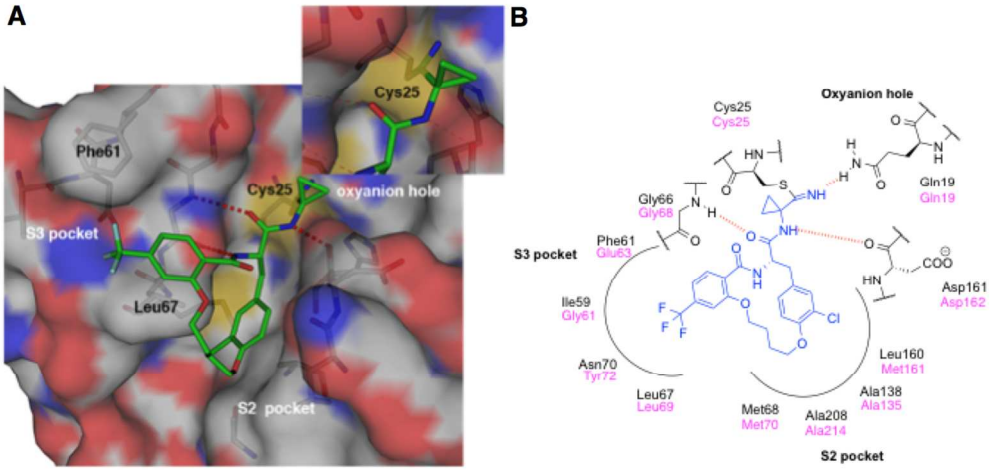

Figure 2. (A) Predicted binding mode of macrocycle 1 in complex with RD (protein coordinates taken from PDB ID: 2P7U33, 1.65 Å resolution). Color code: gray CRD, green Cligand, red O, blue N, yellow S. Atomic surface shown. The insert shows the expected thioimidate formation by the catalytic Cys25. (B) Schematic binding mode of 1, showing the putative covalent bond between Cys25 and the nitrile head group and the stabilization of the formed thioimidate by the oxyanion hole. The residues from RD are labeled in black and the residues from hCatL in magenta. Hydrogen bonds are represented as red dashed lines in (A) and (B).

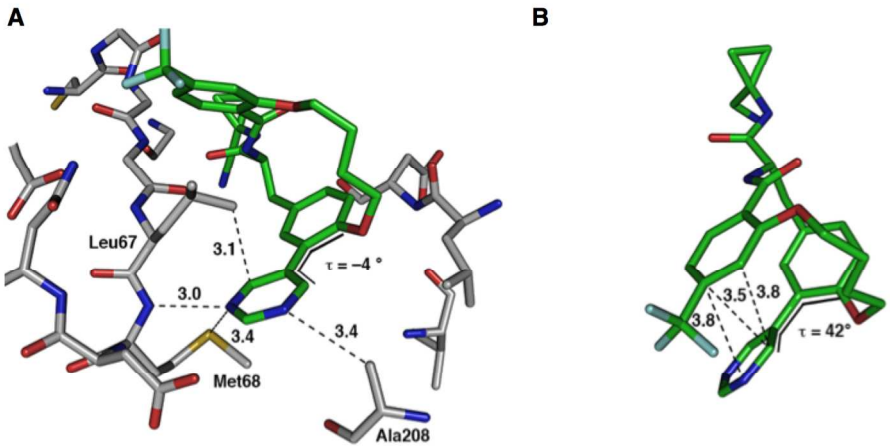

Figure 3. (A) Predicted binding mode of macrocycle 31b in complex with RD (protein coordinates taken from PDB ID: 2P8622, 1.16 Å resolution), highlighting the unfavorable torsion angle τ = −4 ° in the bound state; (B) Macrocycle 31b optimized in the free state, showing a probable hydrophobic collapse of the ligand in solution. The torsion angle τ = 42° in the unbound state is ideal for such biaryl systems.51 Color code: green Cligand, gray Cprotein, red O, blue N, yellow S, cyan F. Distances given in Å.

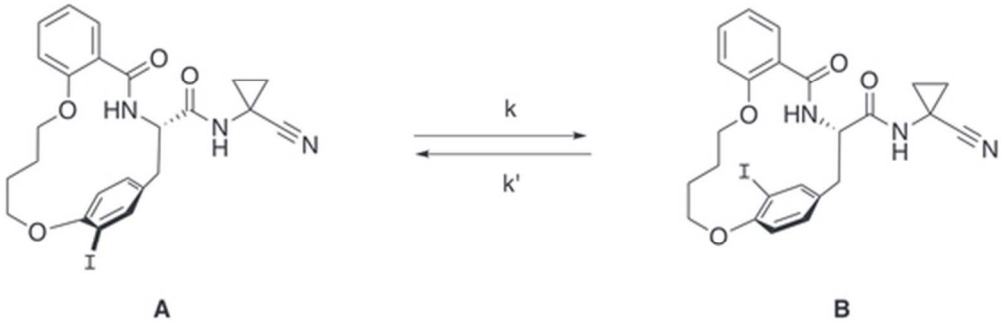

Figure 4. Slow equilibrium between the two diastereoisomeric atropisomers A and B of macrocycle 41. The drawing of compound A depicts the (Rp,S) configuration and the drawing of B the (Sp,S) configuration, assigned according to the rules for planar chirality52 but the configurations were not experimentally assigned. X-ray crystal structures later showed that the (Sp,S) diastereoisomer of the macrocycles is bound exclusively (see below).

46x15mm (300 x 300 DPI)

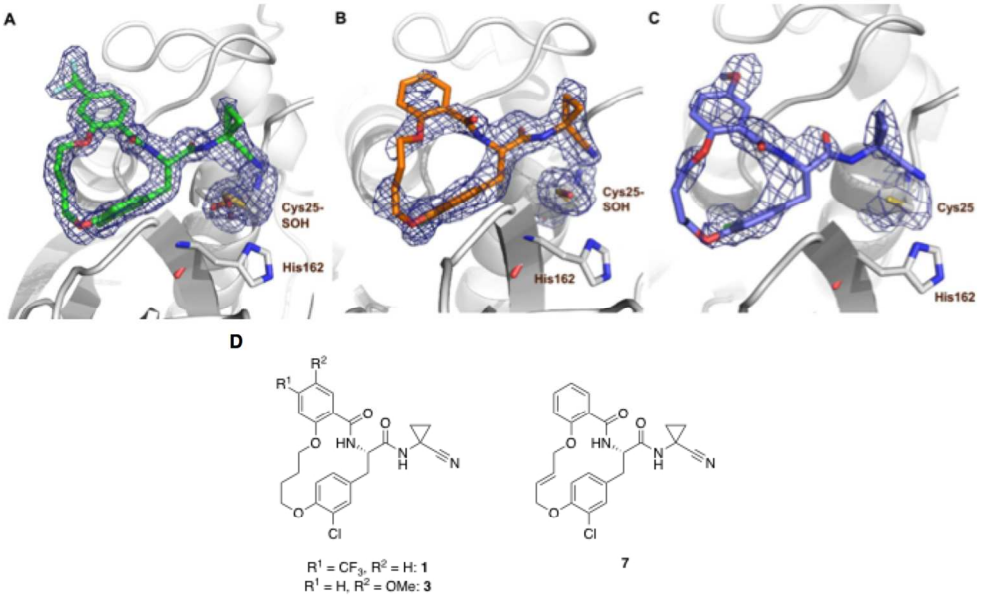

Figure 5. (A) Fo-Fc Electron density map shown as a blue mesh of ligand 1 and the active site cysteine of RD (PDB ID: 6EX8, 1.6 Å resolution). The enzyme is shown in gray and ligand 1 is shown in green. (B) Electron density map of ligand 7 and the active site cysteine of RD (PDB ID: 6EXO, 1.9 Å resolution), the color code is the same as in A, ligand 7 is shown in orange; (C) Electron density map of ligand 3 and the active site cysteine of RD (PDB ID: 6EXQ, 2.5 Å resolution), the color code was maintained, and ligand 3 is shown in violet; (D) Chemical structures of ligands 1, 3, and 7. The Fo-Fc maps were calculated in the absence of the inhibitor and the active site cysteine and are contoured at 2.5 σ. Refinement for Cys25-SOH in (A) was carried out in two different orientations at 50% occupancy each. In (C), the oxidation of Cys25 is not visible due to the lower resolution of the dataset but can be assumed because of the same crystallization conditions for all three structures.

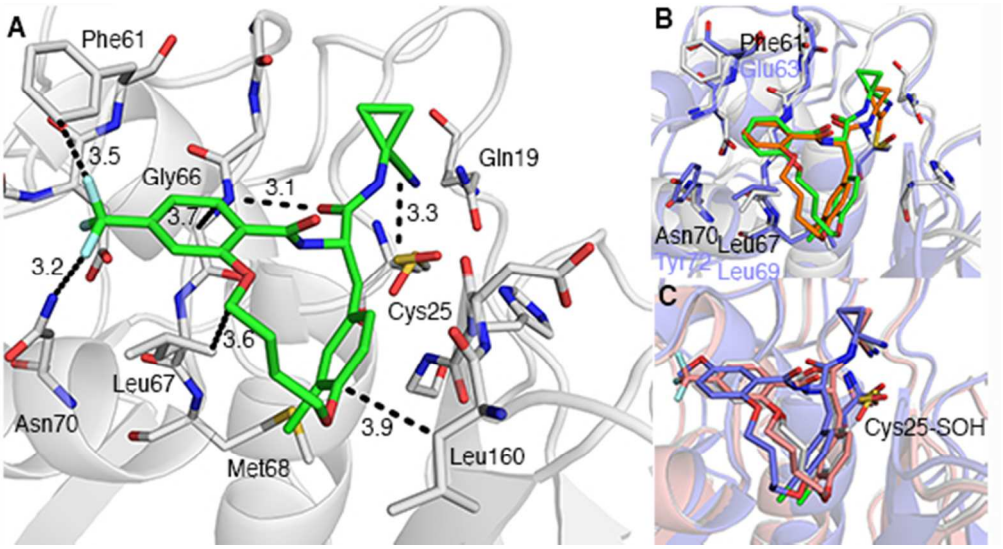

Figure 6. (A) Binding mode of 1 in complex with RD (PDB ID: 6EX8, 1.6 Å resolution), color code: green Cligand, gray Cenzyme; (B) Overlay of the crystal structures of 7 in complex with RD (PDB ID: 6EXO, 1.9 Å resolution) and with hCatL (PDB ID: 6EZP, 2.34 Å resolution), color code: green Cligand,RD, orange Cligand,hCatL, gray CRD, violet ChCatL; (C) Overlay of all three crystal structures of macrocycles 1 (in pink, PDB ID: 6EX8, 1.6 Å resolution), 7 (in gray, PDB ID: 6EXO, 1.9 Å resolution) and 3 (in violet, PDB ID: 6EXQ, 2.5 Å resolution). Common color code: red O, blue N, yellow S. Distances given in Å and represented as dashed black lines.

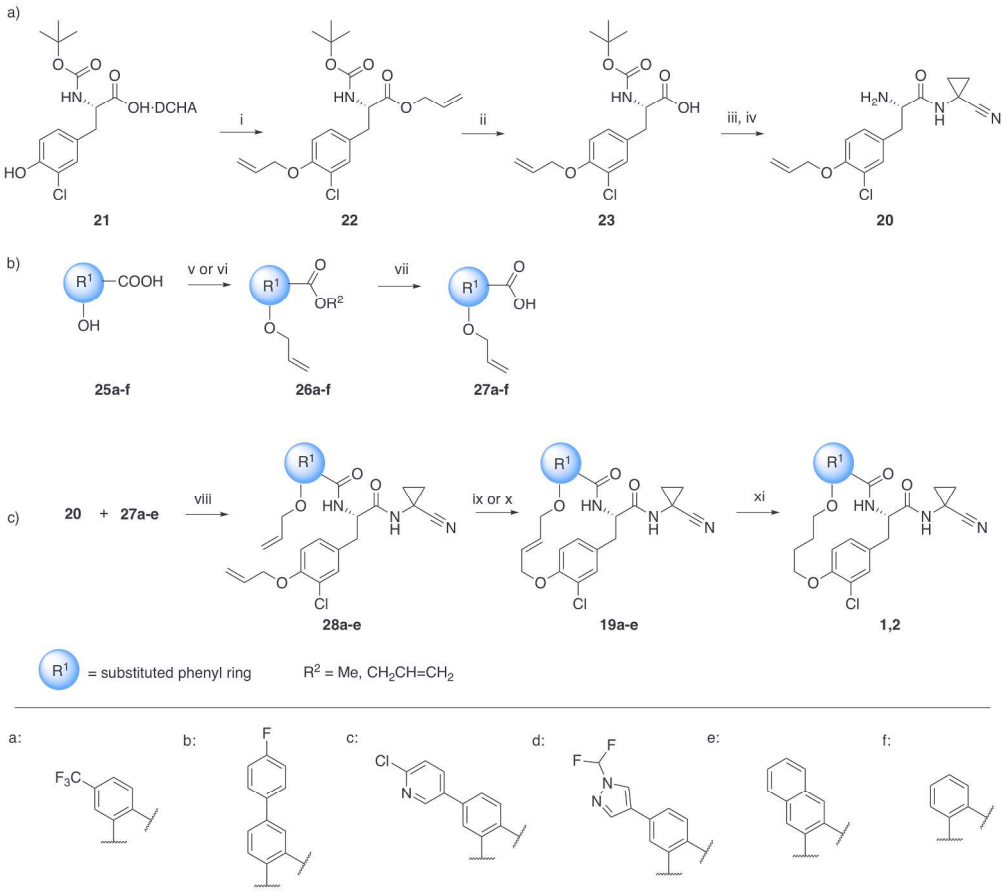

Scheme 1. Synthesis of Macrocycles 1,35 2,35 and 19a–ea

234x207mm (300 x 300 DPI)

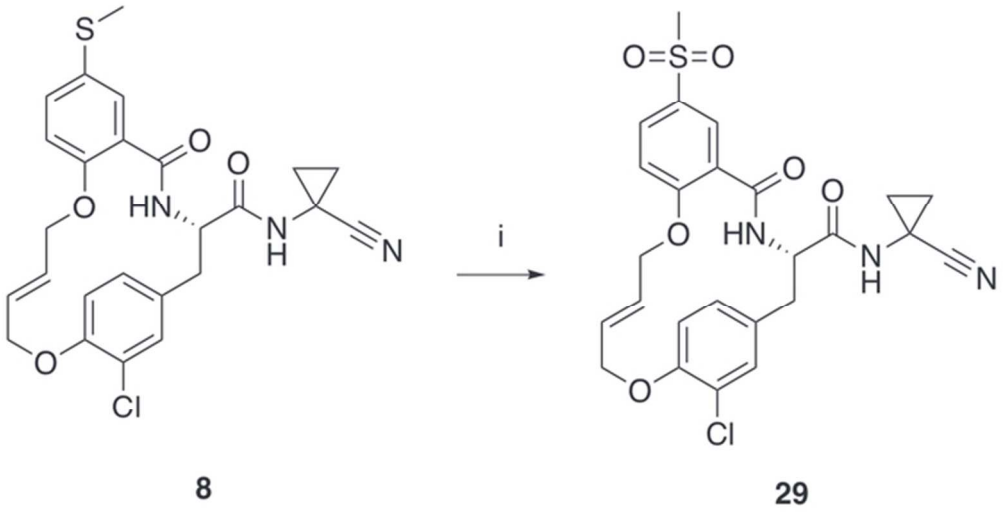

Scheme 2. Derivatization of 29.a

58x29mm (300 x 300 DPI)

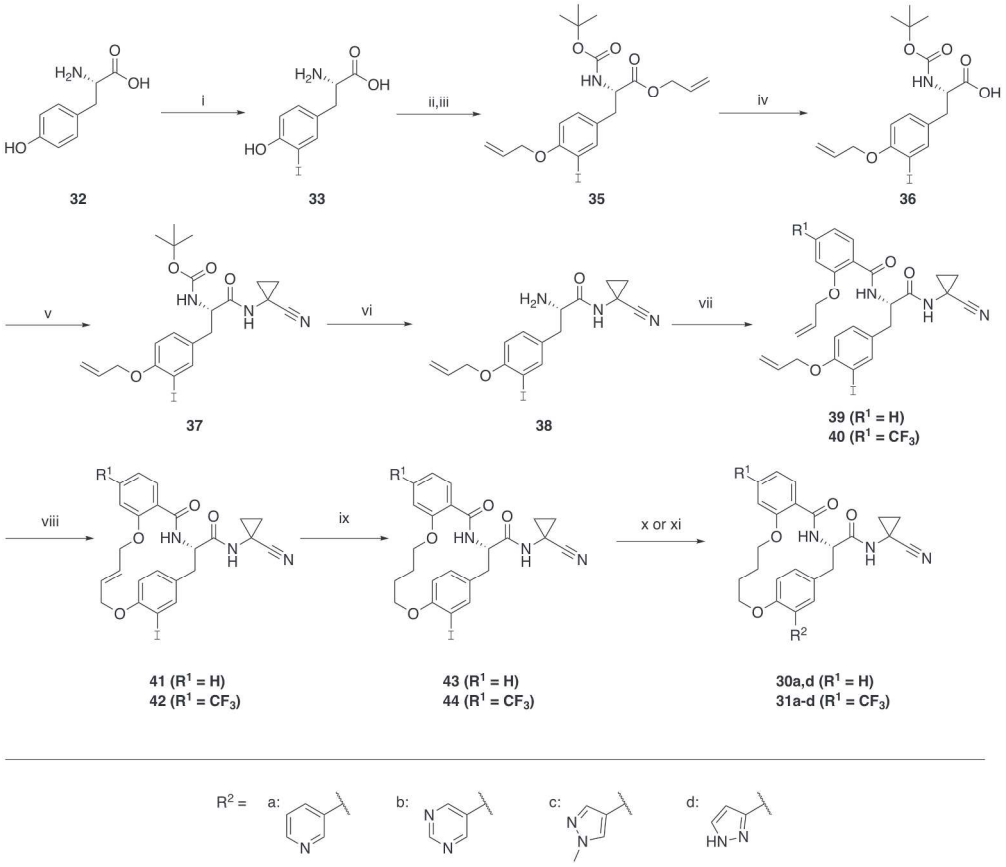

Scheme 3. Preparation of Macrocycles 30a,d and 31a–da

234x202mm (300 x 300 DPI)

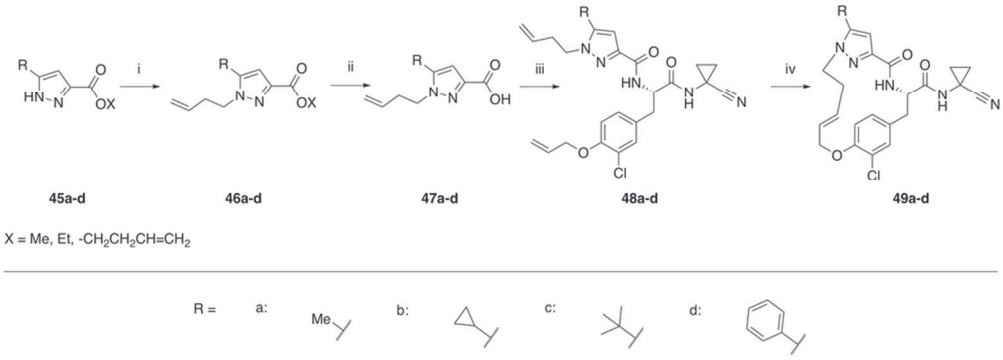

Scheme 4. Preparation of Ligands 49a–d Described in Table 5.

88x31mm (300 x 300 DPI)

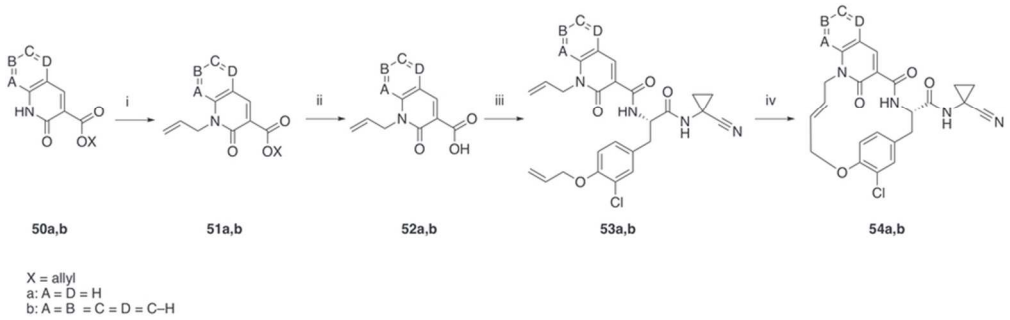

Scheme 5. Preparation of Ligands 54a,b Described in Table 5.

78x24mm (300 x 300 DPI)

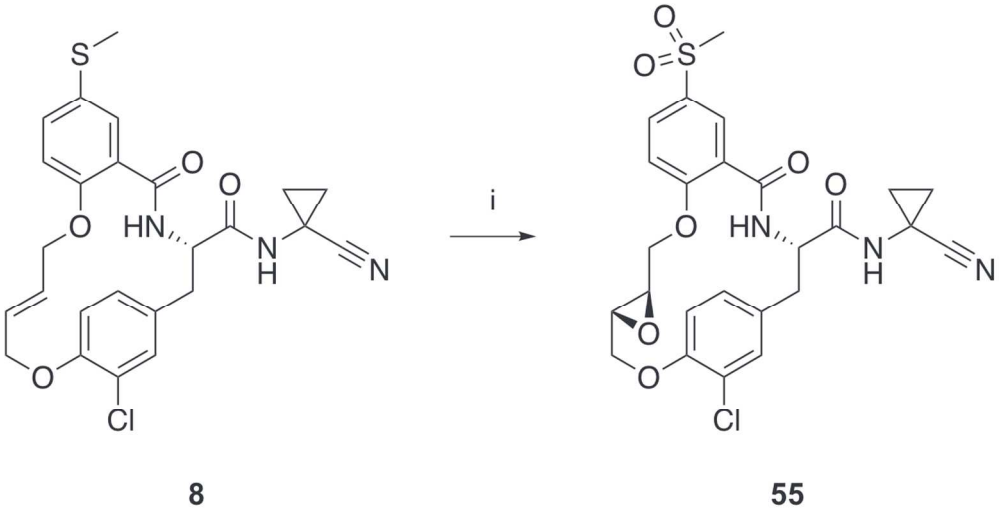

Scheme 6. Derivatization of 835.a

117x60mm (300 x 300 DPI)

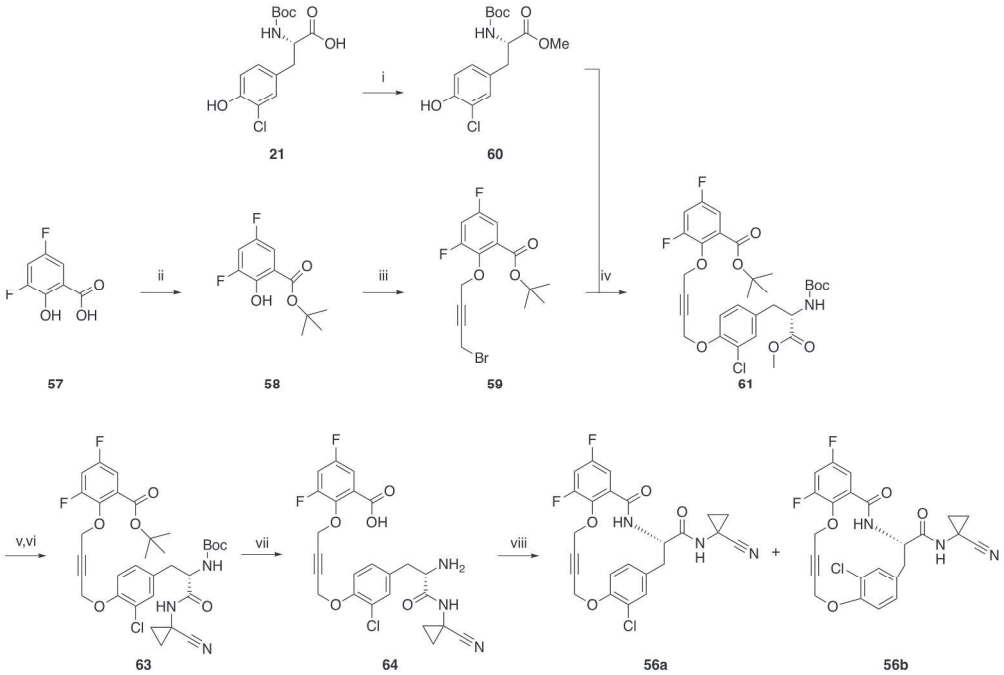

Scheme 7. Preparation of 56a and 56ba

245x163mm (300 x 300 DPI)

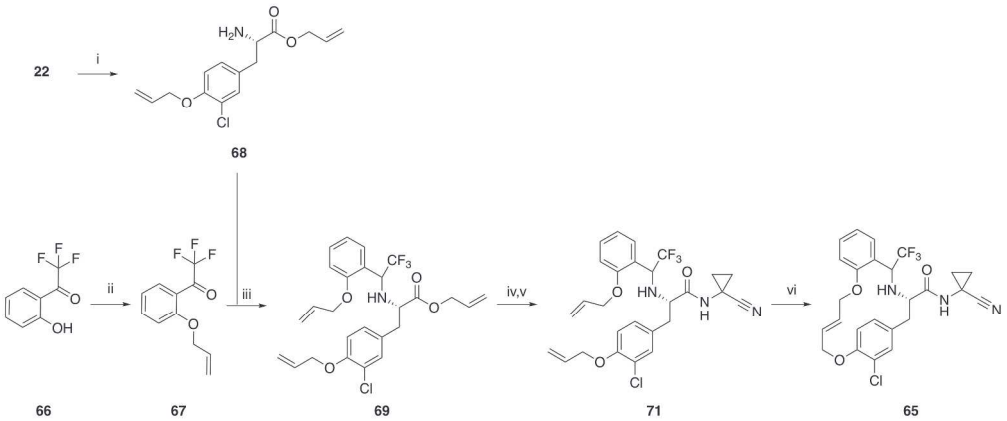

Scheme 8. Preparation of Macrocycle 65.a

252x104mm (300 x 300 DPI)

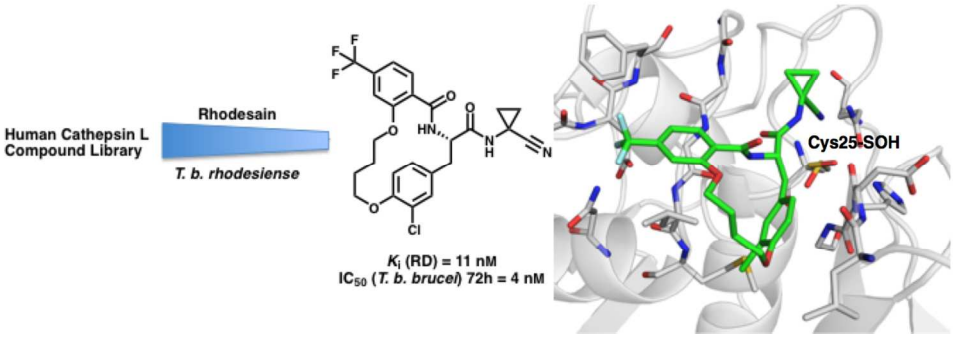

Table of Contents graphic